Non-Equilibrium Synthesis of Highly Active Nanostructured, Oxygen-Incorporated Amorphous Molybdenum Sulfide HER Electrocatalyst

note finali coverpage

(Article begins on next page)

05 February 2025

Non-Equilibrium Synthesis of Highly Active Nanostructured, Oxygen-incorporated Amorphous Molybdenum Sulfide HER Electrocatalyst

Giorgio Giuffredi[1,2], Alessandro Mezzetti[1], Andrea Perego[1,2,§], Piero Mazzolini[1], Mirko Prato[3], Francesco Fumagalli[1], Yu-Chuan Lin[4], Chenze Liu[5], Ilia Ivanov[4], Alex Belianinov[4], Massimo Colombo[6], Giorgio Divitini[7], Caterina Ducati[7], Gerd Duscher[5], Alex Puretzky[4], David B. Geohegan[4], Fabio Di Fonzo[1,*

1. Center for Nano Science and Technology – Istituto Italiano di Tecnologia (IIT@Polimi). Via Pascoli 70/3, 20133 Milano, Italy

2. Department of Energy – Politecnico di Milano. Via Lambruschini 4, 20156 Milano, Italy

3. Materials Characterization Facility – Istituto Italiano di Tecnologia. Via Morego 30, 16163 Genova, Italy

4. Center for Nanophase Materials Sciences – Oak Ridge National Laboratory, Oak Ridge, Tennessee 37831, United States

5. Department of Material Science and Engineering, University of Tennessee, Knoxville, United States

6. Nanochemistry Department – Istituto Italiano di Tecnologia, Via Morego 30, 16130 Genova, Italy

7. Department of Materials Science & Metallurgy – University of Cambridge, 27 Charles Babbage Road, CB3 0FS – Cambridge, UK

ABSTRACT. Molybdenum sulfide is considered one of the most promising non-precious Hydrogen Evolution Reaction (HER) catalysts thanks to its high activity and natural abundance. Despite its remarkable efficiency, the limited number of active sites and the intrinsically low electrical conductivity of most MoS_2 catalyst preparations hamper the potential catalytic efficiency and reaction kinetics. To address the two drawbacks, we use Pulsed Laser Deposition (PLD) for the non-equilibrium synthesis of self-supported, hierarchical nanostructured molybdenum sulfide (MoS_x). Different nanostructures are obtained by sequential attachment of nanocrystalline and highly defective molybdenum sulfide building blocks. The as-synthesized MoS_x shows a nanocrystalline structure, composed of an amorphous matrix with embedded nanodomains of bent and defective S-Mo-S parallel layers, characterized by excess sulfur and segregated molybdenum particles. Incorporation of oxygen through amorphization of the nanocrystalline pristine structure fosters the creation of sub-stoichiometric oxide/oxysulfide phases that, thanks to their high

electrical conductivity, enable a fast electron transfer rate to the active sites. The combined effect of the nanocrystalline structure of the as-synthesized material and the incorporation of oxygen on the surface enhances the performance of the catalyst, resulting in small overpotentials, very fast reaction kinetics (Tafel slope of 35.1 mV dec^{-1}) and, for the optimized MoS$_x$ morphology, a remarkable long terms stability for continuous operation at current density up to -1 A cm^{-2}. Our work shows the possibility in catalytic design that stem from a non-equilibrium synthesis technique like PLD and the importance of structural, chemical and morphological control to improve the HER performance of MoS-based catalysts.

1. Introduction

Production of hydrogen (H$_2$) from water electrolysis[1] or electrocatalytic water splitting[2] represents an attractive and scalable method to store the intermittent electrical energy generated by renewable sources into the chemical bonds of the hydrogen molecule.[3–5] The recognized state-of-the-art catalyst for electrochemical hydrogen evolution reaction (HER) is platinum[6] thanks to its high activity, fast reaction rate and good electrochemical stability. However, the high cost and scarcity of platinum limits its feasibility as a catalyst in a scaled-up hydrogen-based energy economy. Consequently, scientific efforts have been increasingly dedicated to the study and development of earth-abundant, cost-effective, non-precious HER catalysts.[7,8]

Among the many non-precious HER electrocatalysts that have been studied in the literature, transition metal dichalcogenides (TMD$_s$) – in the form MX$_2$, where M is the transition metal (e.g. Mo, W) and X the chalcogen (e.g. S, Se) – are particularly appealing because of their remarkable catalytic activity [9–11]. Particular attention has been addressed to crystalline molybdenum disulfide (MoS$_2$) as the most promising HER catalyst[12] thanks to its electrochemical stability, earth-

abundance, and outstanding HER activity that stems from the nearly optimal thermoneutral value for the calculated binding energy of hydrogen adsorbed on its active sites.[13,14] Moreover, the anisotropic layered structure of MoS_2 presents two distinct crystallite orientations, the basal planes and the edge plane, that exhibit substantially different electrochemical properties:[15] the hydrogen adsorption energy is optimal for the molybdenum atoms on the edge planes, which are the HER active sites, whereas the basal plane is inert towards the reaction.[12,16] Amorphous molybdenum sulfides (a-MoS_x) on the other hand exhibit a variety of defect-rich, partially disordered structures with a high density of under-coordinated sites,[17] whose homogeneous presence in the material can lead to a very high HER activity, as demonstrated in literature.[18,19] Despite their remarkable characteristics, two crucial factors still limit the performance of molybdenum sulfide based HER electrocatalysts: the unsatisfactory electrical conductivity of the material, since the resistivity of c-MoS_2 is in the order of 10^4 Ω cm,[20] and the limited availability of the active sites to the electrolyte. The limited electrical conductivity affects both crystalline MoS_2 (c-MoS_2) and amorphous MoS_x: for c-MoS_2, it is related to the geometrically anisotropic layered structure of c-MoS_2, which causes a sluggish electron transfer rate between different planes of the material[15] and a large bandgap, ranging from 2.40 eV to 1.75 eV depending on the number of layers.[21] For a-MoS_x, instead, the disordered structure itself limits the maximum electron transfer rate and its conductivity. The localization of the HER active sites on the edges of crystalline molybdenum sulfide, moreover, limits the electrochemically active area, since the two basal planes of the layered material are inert. To overcome these drawbacks, two main strategies have been pursued in the literature: either controlling the morphology to maximize the exposure of the active sites and the electrochemical active surface area, or enhancing the intrinsic activity of the catalyst by creating new HER active sites and increasing the electrical conductivity. To increase the active area, researchers maximized

the exposure of the [1010]-Mo edge active sites towards the electrolyte by a variety of approaches: by synthesizing vertically-aligned MoS_2 platelets, either self-supported[22] or supported on a porous carbon-based material;[23] by growing MoO_{3-x}/MoS_2 core/shell nanowires with high density of exposed edge sites;[24] by fabricating 2D structures like nanowalls [25] or 3D morphologies such as nanospheres;[19,26] or by supporting thin MoS_2 catalytic layers on conductive, high-surface-area carbon-based supports.[27–31] Effectively exposing the maximum number of active edge sites leads to a remarkable increase of the catalytic surface area, consequently improving the HER performance of MoS_2 catalysts. On the other hand, in order to enhance the intrinsic activity and conductivity of MoS_2, two approaches are usually employed. The first approach consists in forming new active sites in the pristine material, either by creating new under-coordinated sites in the basal plane through the incorporation of vacancies[32,33] or by transitioning the material into its metallic state with enhanced electrical conductivity and higher density of active sites. [20,34–37] The second approach aims at modifying the electronic structure of the material through doping with different elements,[38–42] thus increasing the catalyst electrical conductivity and achieving a faster reaction rate. In this regard, oxygen incorporation has proved to be an efficient way to improve the electrical conductivity of MoS_2 catalyst and to enhance its HER performance, because sub-stoichiometric molybdenum dioxide (MoO_2) exhibits a metal-like electrical conductivity. In previous reports,[43–47] the incorporation of oxygen in MoS_2 materials led to the compresence of both MoS_2 and MoO_2 phases in the catalyst or to the exploitation of MoO_2 conductive backbones to accelerate the electron transfer to the MoS_2 HER active sites, thus achieving remarkable reaction kinetics and smaller overpotentials. Moreover, the inclusion of oxygen modifies the surface electronic structure of MoS_2, favoring the interaction between active site and reactants and enhancing the electronic transport near the active sites, boosting the catalytic activity.[43,48] For

amorphous molybdenum sulfides, which are usually synthesized by electrochemical or wet-chemical methods with limited control over the final morphology of the deposited materials, coupling the catalyst with conductive supports with controlled morphology is an efficient way to both enhance the conductivity of the catalyst and to finely tune the final architecture of the a-MoS$_x$ material to maximize the surface area. Examples include depositing a-MoS$_x$ on carbon nanotubes (CNTs),[19] N-doped carbon nanotubes,[49] reduced graphene oxide fibers,[50] graphene-CNTs hybrids[51] or p-doped Si nanowires:[52] thanks to these conductive supports whose morphology can be easily controlled, the resulting catalytic architecture achieves enhanced catalytic performances in terms of lower overpotentials – thanks to the high surface area provided by the supporting structure – and faster kinetics – due to the faster electron transfer rate from the conductive support to the active site.

In this work, we exploit a non-equilibrium synthesis by Pulsed Laser Deposition (PLD), to induce the controlled nucleation and condensation of molybdenum sulfide clusters in the vapor phase. By tuning the interaction between the laser generated plasma and the process gas, we can modify the kinetic energy of the clusters upon their landing on the deposition substrate thus controlling their sequential attachment into nanocrystalline, metastable nanostructures characterized by quasi 1D morphology whose porosity can be controlled down to the micro- and nanoscale. We leverage the metastable structure of PLD-grown molybdenum sulfide, whose inherently defective structure at the nanoscale size ensures a wide variety of active sites for the reaction. Moreover, the PLD process allows the synthesis of self-supported MoS$_x$ hierarchical nanostructures with tunable morphology from dense, compact films to porous, hierarchical nanostructures. Previous reports about the synthesis of MoS-based HER catalysts by PLD[53–55] reported the deposition of a-MoS$_x$ thin films on different substrates, with HER

performances in line with those of wet chemical methods. On the other hand, we use PLD for nanoengineering the material from its atomic level up to its micro- and nanoscale morphology. The disruption of any long range order in the as deposited MoS_x facilitate its electrochemical 'activation' process,[56–58] in which the pristine material undergoes an irreversible chemical and structural modification. Indeed, the excess surface sulfur in the as-synthesized MoS_x catalyst is substituted with oxygen, fostering the creation of reduced molybdenum oxide/oxysulfide phases with higher electrical conductivity on the surface of the material, effectively enhancing the HER kinetics through a faster electron transfer rate near the HER active sites.

By exploiting the combined effect of the defective nanoscale organization of the material and the electrochemical oxygen incorporation, we obtain MoS-based HER catalysts that perform the reaction with remarkable activity, characterized by a very fast reaction kinetics thanks to a noteworthy Tafel slope of 35 mV dec^{-1}. By optimizing the nanostructure morphology, we optimize the overpotentials at -10 mA cm^{-2} and -100 mA cm^{-2} with values of 126 mV and 170 mV, we maximize the activity of the catalyst by achieving a remarkable per-site TOF of 3.5-1.2 H^2 s^{-1} at 150 mV, and achieve an unprecedented long-term stability for non-crystalline MoS_x catalysts, with a 100-hour stability after continuous operation at -100 mA cm^{-2} and over 25-hour stability at -1 A cm^{-2}. With this work, we show that by employing out-of-equilibrium synthesis technique as PLD, combined with a precise compositional control achieved through electrochemical methods, it is possible to drastically enhance the HER performance of non-crystalline MoS_x materials, providing the framework for the development of self-supported, non-crystalline and non-precious HER electrocatalysts.

2. Materials and Methods

Substrates. For the PLD synthesis of the MoS_x films, glassy carbon (Tokai Carbon), soda lime glass microscope slides (Thermo Fisher Scientific) and electronic grade silicon (SiMat) are employed as substrates. Glassy carbon is used as the substrate for electrochemical analysis. To create a flat surface on glassy carbon for MoS_x deposition, the substrates are successively polished with 1200 and 2400 sandpaper, then with 1 μm and 0.3 μm alumina paste. Subsequently, they are sonicated in acetone (Honeywell), isopropanol (Honeywell) and distilled water.

Device Fabrication. MoS_x nanostructures are obtained starting from a crystalline MoS_2 target (Testbourne, 99.9% purity). Pulsed Laser Deposition is carried out using a KrF excimer laser (Coherent Gmbh. COMPex 205 F, λ=248 nm), in a vacuum chamber evacuated down to 0.003 Pa, filled with an Ar (99.9999%) atmosphere. The total incident fluence on the MoS_2 target is 3.1 J cm^{-2} $pulse^{-1}$ and the target/substrate distance is 5 cm.

In-situ PLD diagnostics. Plume imaging was performed with an ICCD camera (Princeton Instruments, PI-MAX) with variable gating. A Nikon camera lens was positioned outside the chamber, focusing on the plasma plume through a Suprasil window, varying the exposure time and f-stop according to the plume conditions. The ion probe time-of-flight measurements (detector area 1 mm^2) were acquired during the deposition process, adjusting the resistor across which the current is measurement according to the plasma conditions.

Morphological Characterization. Cross-sectional images are acquired with a Zeiss SUPRA40 field-emission scanning electron microscope (SEM), with an operating voltage of 5 kV and a working distance of 2 mm. Brunauer–Emmett–Teller (BET) area measurements are carried out in a Quantachrome Instruments Autosorb iQ gas sorption analyzer, after outgassing the samples at

30°C for 180 min. Pore size distributions were calculated using the Barrett-Joyner-Halenda (BJH) method.

Structural Characterization. High frequency Raman spectra are acquired with a Renishaw InVia Raman Microscope, using a 532 nm excitation laser line with an incident power of 0.37 mW. Low frequency Raman spectra are acquired with a Renishaw inVia micro-Raman system with a 532 nm excitation line. XRD patterns are acquired with a Bruker D8 Advance diffractometer in a grazing-incidence geometry. A Cu Kα_1 (λ = 1.54406 Å) anode, operating at 40 kV and 40 mA, was employed. All the diffraction patterns are acquired at room temperature, with an angular position of the anode of 1°, over an angular range 10°-80°. The step size was 0.01°, the acquisition time was 2 s for each step. TEM samples are prepared by scratching nanoparticles from substrate and then transferring to lacey carbon TEM grid. High-resolution transmission electron microscopy (HR-TEM) micrographs and selected area electron diffraction (SAED) patterns are obtained with a Carl Zeiss LIBRA 200MC TEM operated at 200 kV. The high-angle annular dark-field scanning transmission electron microscopy (HAADF-STEM) and core-loss EELS characterization is conducted using a Nion Ultra STEM 200 microscope operated at 200 kV. Before STEM observation, the TEM grids were baked at 160 °C for 8 h in vacuum. All core-loss EELS spectra are quantitatively analyzed using the Quantifit software.[59] EDX compositional maps are obtained with a FEI Tecnai Osiris Scanning/Transmissione Electron Microscope (S/TEM) operated at 200 kV. X-ray Photoelectron Spectroscopy (XPS) analyses are carried out using a Kratos Axis Ultra[DLD] spectrometer (Kratos Analytical Ltd., UK). XPS spectra are acquired using a monochromatic Al K$_\alpha$ source operated at 20mA and 15 kV. The analyses are carried out on 300x700 µm areas. High resolution spectra were collected at pass energy of 10 eV and energy step of 0.1 eV, and the Kratos charge neutralizer system was used on all specimens. Spectra have been charge-corrected to the

main line of the C 1s spectrum set to 284.8 eV and analysed with CASAXPS software (Casa Software, Ltd., version 2.3.17).

Helium Ion Microscopy with Secondary Ion Spectrometry (HIM-SIMS) analysis is performed on a Carl Zeiss ORION NanoFab. Helium Ion Microscopy with Secondary Ion Spectrometry (HIM-SIMS) is a relatively new technique that combines the high-resolution imaging of the HIM with the chemical sensitivity of SIMS.[60,61] The HIM is a gas field ion source based focused ion beam capable of operating with helium and neon gas, and offering beam spot sizes of 0.5 nm and 2 nm respectively. The SIMS add-on unit allows detection of the ion distribution with a spatial resolution of ca. 15 nm.[62] HIM-SIMS operates via a double-focusing magnetic sector, capable of mass resolution of ~500. The ion extraction system is fully retractable and the HIM can be used in secondary electron detection mode without being affected. HIM-SIMS micrographs for the pristine MoS_x are reported in the Supplementary information.

Electrochemical Methods. Electrochemical measurements are carried out in a one compartment, 3-electrode cell (Pine Instruments) utilizing a 0.5 M H_2SO_4 aqueous electrolyte. Sulfuric acid purchased from Sigma-Aldrich and ultrapure water (Millipore) are employed for electrolyte preparation. The electrolyte was purged from residual O_2 with nitrogen for approximately 20 minutes before electrochemical experiments. A platinum spiral is employed as counter electrode and an Ag/AgCl (saturated KCl) was used as reference electrode. As reference for the linear sweep voltammetry (LSV) measurements, two different Pt references are employed: a Pt mesh and a commercial Vulcan XC72-supported Pt GDE, with a Pt loading of 0.2 mg cm^{-2} (Fuel Cell Store). A control linear sweep voltammetry (LSV) experiment is carried out employing a carbon 29AA GDL (Sigracet) as counter electrode to rule out any hypothetical Pt contamination on the working

electrode.[63,64] The Ag/AgCl to RHE potential conversion is obtained through the following equation:

$$E_{RHE} = E_{Ag/AgCl} + 0.197 + 0.0591 \cdot pH$$

The electrochemical activation process is triggered by performing 30 cyclic voltammetry scans between -0.2 V_{RHE} and 0.5 V_{RHE}, with a scan rate of 150 mV s^{-1}. LSV are performed with a scan rate of 5 mV s^{-1} and iR correction is performed utilizing the high frequency, series resistance extrapolated by electrochemical impedance spectroscopy (EIS) measurements. EIS spectra are acquired at a fixed current density of -10 mA cm^{-2} from 10 kHz to 10 mHz. All electrochemical measurements are performed with an Autolab Multi-Autolab M204 potentiostat. For the fitting and the simulation of EIS spectra, the built-in tool of Autolab NOVA 2.1 software is employed. In plotting the voltammograms, the current is normalized to the geometrical area of the sample of 0.19635 cm^2 and the current density is indicated in the units of mA cm$^{-2}_{geo}$. When the current is normalized to the effective, 3D surface area of the sample, the current density is indicated in mA cm$^{-2}_{eff}$.

3. Results and Discussion

3.1. Non-Equilibrium Synthesis by Pulsed Laser Deposition

The MoS$_x$ nanostructured films are synthesized by exploiting the non-equilibrium characteristics of Pulsed Laser Deposition (PLD) of a crystalline MoS$_2$ target. The target is placed in a vacuum chamber filled with a background gas – in this case Argon – and is ablated with UV light pulses from an excimer laser (KrF, 248 nm, 3.1 J cm^{-2}) to deposit on a substrate at room temperature, placed at a distance of 5 cm from the ablated target. When hit by the laser pulses, the target material is vaporized and partially ionized, supersonically expanding as a visible plasma plume

from the target surface towards the facing substrates. The ablated species then condense and impinge on the substrates surface, gradually growing the film. During the deposition, nucleation of nanoparticles and clusters of the material inside the plasma plume can be induced and tuned by controlling the pressure of the background gas, consequently controlling the deposition mechanism and the growth of the nanostructures. Moreover, with PLD it is possible to finely control the morphology over the synthesized films morphology down to the micro- and nanoscale, with the ability to obtain hierarchical quasi-1D nanostructures with high surface area [65–67] or hyperbranched morphologies with controlled aspect ratio. [68–70]

Our PLD synthesis of MoS_x films is carried out employing three different argon pressures, namely 5 Pa, 10 Pa and 30 Pa, to evaluate how the interaction between the non-equilibrium plasma and the different gas pressures affects the dynamics of the plasma plume, the clustering of the nanoparticles in the plume edge and their landing on the substrate. Plasma dynamics in these deposition conditions is studied *via in-situ* diagnostics, i.e. ion probe time-of-flight current measurements and intensified charge couple device (ICCD) imaging and summarized in **Figure 1**. The ablation of the c-MoS_2 target results in the formation of a plasma plume rapidly expanding in the forward direction, composed by distinct components whose relative intensity depends on the interaction with the background gas, where four components are identified. A first 'dark' component, not visible in the ICCD images but still being distinguished by the ion probe, is composed of atoms and ions characterized by high kinetic energy that penetrate the background gas without interacting with it. This first component can be clearly distinguished in the plot in **Figure 1b**, as it is registered by the first peak at ~7 µs. A second main component, identified in the purple region in **Figure 1a-c**, is composed of a high number of atoms, molecules and nanoparticles in the plasma and dominates for the deposition at lower pressures. The third

component is a generated by a 'rebound' of the plasma plume against the substrate (green region in **Figure 1a-c**): many of the nanoparticles of the main plasma component do not attach to the substrate upon contact. Instead, due to their high kinetic energy, they bounce back towards the target after interaction one with another inside the plasma. Finally, a fourth 'tail' component (red region in **Figure 1a-c**), composed of heavier clusters and nanoparticles characterized by much slower velocity than the previous three, is present in the last part of the plasma plume. Apart from delivering to the substrate the heavier material clusters, the tail component interacts with the rebound particles moving backwards, further promoting the aggregation and the formation of the clusters that compose the PLD-synthesized films.

These four components are influenced differently by the changes in Ar pressure. The velocity of the first 'dark' plasma component is not affected by the increasing gas pressure, since its arrival time is roughly the same, ~ 7 μs for the lower Ar pressures (5 Pa and 10 Pa) and for PLD in vacuum (**Figure SI 1**). The main component, instead, along with the 'rebound' and 'tail', are increasingly slowed down by the background gas pressure and their arrival time on the substrates is delayed: as an example, the arrival time of the main component is delayed from 8 μs (MoS_x 5 Pa) to 18 μs and 35 μs for MoS_x 10 Pa and 30 Pa respectively. The splitting of these two parts of the plume is described in detail in other works [71,72] and follows a scattering model which describes the collisions of the atoms and nanoparticles in the plasma plume with the background gas. For increasing background gas pressure, the slowing of the plume is associated to a decrease in kinetic energy of the particles in the plasma, as shown by the difference in ion probe currents between the 5 Pa or 10 Pa (**Figure 1a-b**) which range from 300 μA and 500 μA, and the 30 Pa plume (**Figure 1c**), where the ion current decreases by one order of magnitude, with a maximum of roughly 30 μA.

Moreover, along with the strongly diminished kinetic energy, for the highest Ar pressure the fast 'dark' component disappears, as revealed by the ion probe currents in **Figure 1c**.

The plumes propagating at different Ar pressures are dominated by different components. At the lowest pressure of 5 Pa, the 'dark' and 'main' component are the dominant ones and arrive on the target at a similar time, while the 'tail' component is characterized by a very modest intensity. The first 'dark' component is instead diminished in intensity for the 10 Pa plasma, where the dominant components are the 'main' one and the 'rebound', characterized by kinetic energies comparable to the 5 Pa plasma. For this Ar pressure, the splitting of the plume components can be fully appreciated and, more interestingly, an interaction between the rebound and the tail component can be seen: the particles that have bounced on the substrates and are moving in the backward direction interact with the heavier and slower aggregates that constitute the tail component, moving back again towards the substrate. The highest pressure of 30 Pa strongly confines and slows down the plasma plume, markedly attenuating the kinetic energy of all its components and – as previously mentioned – causing the disappearance of the dark component. In these conditions the slowing of the plume is evident, with almost doubled plasma arrival times to the substrate, and the tail component is characterized by a comparable kinetic energy to the main one. This transition in the main component of the plasma plume with increasing Ar pressure is related to a change in the growth regime of the PLD-synthesized nanostructures, because a change in the kinetic energy of the material clusters impinging on the substrate leads to different morphologies formed through the sequential attachment of the nanoparticles.

The SEM cross-sectional images in **Figure 2** show the evolution in morphology and porosity of the PLD-synthesized MoS_x nanostructures with different Ar pressures, with a representative thickness of 1 μm, where an increase in Ar pressure leads to an increasing porosity of the film.

The MoS_x film deposited at the lowest Ar pressure of 5 Pa (MoS_x 5 Pa) is shown in **Figure 2a**: PLD with this background gas pressure was dominated by the first dark component and the main one, constituted by species with high kinetic energy landing on the substrate to grow the film. Consequently, this film presents a compact structure, composed of packed nanometric aggregates of material with very limited porosity. As the pressure is increased to 10 Pa the plume splitting phenomenon and the interaction between rebound component and tail component are more evident and the resulting film (MoS_x 10 Pa, **Figure 2b**) is characterized a nanostructured morphology with small openings, with the presence of columnar-like elements with limited inter-columnar spacing. For the higher Ar pressure of 30 Pa (MoS_x 30 Pa, **Figure 2c**), the disappearance of the fast dark component and the marked decrease in kinetic energy of the plume components promotes the growth of less dense, hierarchical elements by subsequent landing of aggregates of nanoparticles weakly attached one another and characterized by bigger size. This nanostructure is composed of widely spaced structures characterized by high porosity, resembling a 'forest of nanotrees' with large inter-columnar spacing and higher surface area than the other two MoS_x morphologies. The evolution in morphology and the formation of nanostructured elements with increasing process gas pressure finds a correspondence in the different kinetic energy of the ablated particles during PLD: as the process gas increases, the nanometer-sized ablated particles land on the substrates as aggregates with increasing size in order to adjust the final porosity of the resulting nanostructured film, as reported in other works.[70]

The porosity features and higher surface area in the MoS_x nanostructures with higher Ar pressure, qualitatively assessed by SEM imaging, are confirmed by the gravimetric and BET surface area values, shown in **Figure 2d**. The BET surface area (black trace) increases with increasing Ar pressure, ranging from 4.7 m^2 g^{-1} for MoS_x 5 Pa to 17.5 m^2 g^{-1} for MoS_x 10 Pa and

$65.2 \ m^2 \ g^{-1}$ for MoS$_x$ 30 Pa. The increase in surface area is concomitant to a decrease in density (red trace), which diminishes as the structure gets more porous starting from a value of $2.93 \ g \ cm^{-3}$ for MoS$_x$ 5 Pa to $2.09 \ g \ cm^{-3}$ for MoS$_x$ 30 Pa. As a comparison, density for bulk, semiconducting MoS$_2$ is $5.06 \ g \ cm^{-3}$. The two concomitant trends suggest that the film porosity is related to a rarefaction of the material, with a bigger void fraction per unit volume in the nanostructured films with higher surface area, synthesized with higher argon pressure. The BET-derived roughness factor RF$_{BET}$ (blue trace), i.e. the surface area per unit volume of material (calculated as the product between BET surface area and density) numerically translates the previous concept, increasing with Ar pressure although with a smaller slope between 10 Pa and 30 Pa than between 5 Pa and 10 Pa. The smaller slope at higher Ar pressure is caused by a decrease in density of the MoS$_x$ films and to the weaker interconnections between the clusters composing the MoS$_x$ 30 Pa nanostructure. The evolution of the nanostructure growth regime with increasing gas pressure finds a correspondence also in the pore size distribution of the MoS$_x$ morphologies, reported in **Figure 2e** after extrapolation from the BET measurements through the BJH method. The two more compact morphologies (MoS$_x$ 5 Pa and MoS$_x$ 10 Pa) share a similar total pore volume, with mean pore size of ~4-8 nm and similar size distribution, although MoS$_x$ 10 Pa shows a slightly higher pore volume in the region below 10 nm. The 30 Pa morphology instead exhibits a different pore profile, with bigger mean pore size, total volume and bigger quantity of pores in the 10 nm–100 nm size range. Therefore, for the more open morphology the larger BET surface area is related to wider inter-columnar spacing and bigger internal pores.

The background gas pressure influences only the morphology of the pristine MoS$_x$ films, while their composition is roughly independent on the Ar pressure. The three MoSx morphologies are characterized by similar molybdenum-sulfur coordination, as confirmed by the Raman spectra

collected in **Figure SI 2a** which show the presence of the same vibrational bands for all the films. The MoS_x nanostructured films show the typical Raman signature found for other amorphous MoS-based materials reported in the literature, where the bands observed at 800 cm^{-1} – 1000 cm^{-1} are ascribed to the presence of MoO_3 on the film surface after its manipulation in atmosphere. The diffractograms in **Figure SI 2b** show the X-ray amorphous nature of the three pristine MoS_x nanostructures, since the characteristic peaks of c-MoS_2 are not present. However, other features with low intensity are registered at 2θ angular positions corresponding to the peaks of metallic molybdenum, as confirmed by the reference pattern reported in the plot.

3.2.　　　HER Catalytic Performance

The influence of MoS_x nanostructures morphology on their HER performance is evaluated through linear sweep voltammetry (LSV) measurements on films characterized by different thickness and porosity. The effect of these two morphological features is then evaluated on the following electrochemical figures of merit: the overpotentials at -10 mA cm^{-2} (η_{10}) and the Tafel slope from the linear fit of the curve in the Tafel plot.

Before the HER testing, the electrochemical 'activation' process is triggered on the different MoS_x catalysts by performing cyclic voltammograms in a potential range defined in Section 2 and visualized in **Figure SI 3a-c**, where the 1 μm-thick nanostructures are considered as an example. The 'activation' process that amorphous molybdenum sulfide materials undergo upon applied electrical potential in an electrolyte is well known in the literature[17,73,74] and transforms the as-prepared a-MoS_x into the actual HER catalytic material. Previous studies have associated the reductive peaks, occurring on the material when the potential is swept cathodically for the first time and irreversible in nature, to either a $S_2^{2-} \rightarrow S^{2-}$ conversion, or to the reduction of defects in the molecular organization of the amorphous material.[56–58,75] In our case, the chosen potential

17

range allows not only to visualize these irreversible reduction peaks, but also to cover an oxidative potential window that promotes the incorporation of oxygen through the formation of sub-stoichiometric molybdenum oxide phases, which according to the Mo Pourbaix diagram are thermodynamically favourable at that potential.[76]

Figure 3 shows the influence of the MoS_x morphological parameters of thickness and porosity on the HER performance descriptors η_{10} and Tafel slope. Increasing the thickness of the nanostructures has a positive effect on the -10 mA cm^{-2} overpotential, as can be distinguished from the trends in **Figure 3a-c**: the 100 nm-thick MoS_x films have similar η_{10} values ranging from 175 mV to 189 mV, slightly smaller for the lowest Ar pressure. As the thickness is increased to 1 µm, η_{10} is shifted to smaller values, with overpotentials ranging from 126 mV for MoS_x 10 Pa to 157 mV for MoS_x 30 Pa. A subsequent increase in thickness to 2 µm leads to a general η_{10} decrease, albeit with a more modest effect than what is seen for the 100 nm–1 µm transition, as for the 2 µm-thick nanostructures the overpotentials lie in a similar 129 mV–140 mV range to the 1 µm-thick MoS_x. The overpotential/thickness relation follows a precise trend: the overall surface area exposed to the electrolyte is higher as the MoS_x films increase in thickness, and consequently a smaller overpotential is required to generate a current density of -10 mA cm^{-2}. The dependence of the HER kinetics on the thickness follows instead a different trend, as visualized by the extrapolated Tafel slope values reported in **Figure 3d-f**. The three 100 nm-thick MoS_x nanostructures are all characterized by Tafel slope values of ~35 mV dec^{-1}, irrespectively of the Ar pressure employed during deposition, and no effect of porosity on the reaction kinetics can be appreciated for this thickness. As the thickness is increased to 1 µm the two more compact MoS_x morphologies, MoS_x 5 Pa and MoS_x 10 Pa, still exhibit Tafel slopes similar to the 100 nm-thick films, with values of 37.3 mV dec^{-1} and 35.1 mV dec^{-1} respectively. On the other hand, for the

more porous MoS_x 30 Pa nanostructure a worse Tafel slope of 43.1 mV dec^{-1} is registered. Finally, for a film thickness of 2 µm, all the three MoS_x nanostructures display worse kinetics, with Tafel slope values ranging from 41.8 mV dec^{-1} (for MoS_x 10 Pa) to 48.9 mV dec^{-1} (for MoS_x 5 Pa).

The η_{10} overpotential strongly depends on the thickness and porosity of the nanostructures, as shown by the previously outlined trends: in general, thicker nanostructures reach a smaller η_{10} value. This trend is easily explained through the definition of η_{10}, i.e. the overpotential required to generate a geometrical, projected current density of -10 mA cm^{-2}, which does not take into account an eventual three-dimensional topology of the catalyst that increases its actual surface area per unit projected geometrical area. A higher ratio between effective, 3D surface area and projected geometrical area that is achieved by thicker or more porous nanostructures likely leads to a smaller value of the η_{10} parameter. Indeed, synthesizing a catalyst with a complex 3D architecture – e.g. through the incorporation in the catalytic system of a support with controlled morphology – is a widespread and efficient method to increase the catalyst surface area in contact with the electrolyte and thus reach a smaller -10 mA cm^{-2} overpotential. Even without a support with controlled morphology, the 1 µm-thick MoS_x 10 Pa catalyst achieves a remarkable η_{10} value of 126 mV, the best result obtained by a self-supported amorphous MoS_x catalyst as reported in **Table SI 2**.

The beneficial influence of the effective, 3D surface area on the LSV curves is taken into account by normalizing the current density not according to the geometrical area but according to the effective 3D surface area, which is represented by the electrochemical roughness factor, RF_{ec}. The average RF_{ec} values are shown in **Figure 4a** and the resulting, effective-area-normalized LSV curves are plotted in **Figure SI 4a-c**. When the effective 3D surface area is considered, the corresponding current density changes considerably from the geometrical-area-normalized current density and a new trend can be observed: for the three thicknesses, the more compact 5 Pa

morphology always shows the best catalytic performance in terms of maximum current density and smaller η_{10} overpotential. The larger RF_{ec} of the 10 Pa and the porous 30 Pa morphologies with 1 μm and 2 μm thickness leads on the one hand to a better catalytic performance when the geometrical-area-normalized current density is considered, while on the other hand to a diminished efficiency when the effective area is taken into account. While increasing the effective, 3D surface area is an efficient method to maximize the exposed active sites and enhance the catalytic efficiency, the more compact MoSx 5 Pa morphology presents still exhibits a remarkable activity even if its surface area is limited.

Differently from the η_{10} parameter, the HER kinetics expressed by the Tafel slope is an intrinsic property of the catalyst independent on its morphology. Hydrogen evolution in acidic media proceeds through two elementary steps: the first one is the Volmer adsorption step, following by either the Heyrovsky or Tafel recombination steps.[77,78] Since the three steps are characterized by specific Tafel slope values,[79] extrapolation of this value gives insight on the HER mechanism occurring on the catalyst and the velocity of the reaction rate determining step. While the Tafel slope values of all MoS_x morphologies can be related to a Volmer-Heyrovsky HER mechanism, where the rate determining step is the Heyrovsky one (characterized by a theoretical Tafel slope of 40 mV dec^{-1}), a marked difference is observed between the more compact MoS_x films and the more porous ones. The three 100 nm-thick MoS_x films and the two more compact MoS_x nanostructures with 1 μm thickness, MoS_x 5 Pa and MoS_x 10 Pa, have Tafel slopes smaller than 40 mV dec^{-1}, with an average value of ~35 mV dec^{-1}, indicating that the Heyrovsky step is performed at a faster rate in comparison to the standard. On the other hand, the more porous, 1 μm-thick MoS_x 30 Pa and the three 2 μm-thick nanostructures are all characterized by worse Tafel

slopes, ranging from 43.1 mV dec^{-1} to 48.9 mV dec^{-1}, indicating a slower speed for the Heyrovsky step and a sluggish kinetics.

Figure 4 shows the influence of MoS$_x$ morphological features on the catalytic activity descriptors of electrochemical roughness factor and charge transfer resistance. Firstly, the calculated electrochemical roughness factor (RF$_{ec}$) is considered in **Figure 4a**, whose measurement procedure is detailed in the Supplementary Information. The parameter represents the ratio between the effective, 3D active area of the catalyst and the its projected area on the substrate and takes into account the surface area of the actual catalyst after its 'activation' process and the chemical/structural modifications that it induces. As expected, an increase in either thickness or porosity (represented by a higher Ar pressure) leads to higher RF$_{ec}$ values: the opening of the MoS$_x$ structures with increasing porosity or, analogously, their increasing thickness allows for a broader surface of contact between the material and the surrounding electrolyte. For the 100 nm-thick films, the effect of porosity on electrochemical roughness factor is limited and the RF$_{ec}$ values are similar for the three MoS$_x$ materials. The weak RF$_{ec}$/porosity dependence for thin nanostructures is explained through the growth regime of PLD-synthesized nanostructures, as described in detail in another work:[80] the neighbouring, nanostructured elements of PLD-grown films are composed of nanoparticles aggregates that during the synthesis, by sticking to one another, confer to the elements their typical 'treelike' shape. The interaction between neighbouring, developed 'nanotree' elements then confers to the film its porosity features and is influenced by the background gas pressure during deposition. Therefore, in the first growth stages nanostructured elements the 'trunk' of the 'nanotree' is formed, the interaction between the 'nanotrees' is low and the porosity features due to the neighbouring 'nanotrees' are still limited. Consequently, the 100 nm-thick films are mostly composed of weakly interacting elements and

the overall porosity is limited, irrespective of the Ar pressure. The MoS_x films porosity features are instead fully developed for a thickness of 1 μm and 2 μm, and the variation in Ar pressure leads to marked changes in RF_{ec}. For both thicknesses, the increase in RF_{ec} is steeper for the MoS_x 5 Pa/MoS_x 10 Pa transition, while the slope of the curve is less pronounced as the nanostructured film gets more and more porous at the 10 Pa/30 Pa transition. The morphology of the MoS_x catalysts affects also the charge transfer resistance (R_{CT}) of the catalysts, as shown in **Figure 4b**. The R_{CT} is extracted by the EIS spectra, which after collection are fitted with an equivalent circuit model employed in the literature for MoS-based catalysts[51,81] visualized in **Figure SI 5**. According to this model, the circuital elements that describe the dominating semicircle (Q_2, R_{CT}) of the Nyquist plot are attributed to the HER occurring on the catalyst, while the elements describing a smaller semicircle (Q_1, R_1) describe non-Faradaic phenomena on the electrode like a distributed resistance/capacitance in the catalyst. The morphology/R_{CT} dependence well matches the Tafel slope trend described in the previous paragraphs. The 100 nm-thick MoS_x films show R_{CT} of 8.6 Ω for MoS_x 5 Pa, 8.4 Ω for MoS_x 10 Pa and 8.6 Ω for MoS_x 30 Pa: the small morphological changes induced by the different Ar pressures at this thickness are reflected by similar R_{CT} values, similarly to the Tafel slopes for the HER. As the thickness is increased to 1 μm the two more compact morphologies, MoS_x 5 Pa and MoS_x 10 Pa, still show similar R_{CT} with values of 8.2 Ω and 7.8 Ω respectively, while the more porous MoS_x 30 Pa film is characterized by a worse R_{CT}, with an extrapolated value of 11.3 Ω. The trend of Ar pressure on R_{CT} is maintained for the 2 μm-thick MoS_x nanostructures, although with worse values: indeed, R_{CT} of 9.8 Ω and 9.3 Ω are obtained for the MoS_x 5 Pa and MoS_x 10 Pa films, while the MoS_x 30 film shows a higher R_{CT} of 11.0 Ω.

To quantify the catalytic activity of the MoS_x nanostructures the exchange current density j_0 is calculated, since its value represents the kinetic facility of the HER redox couple on the catalytic surface and is thus an indicator of the 'reactivity' of the catalyst, according to the following formula.[82]

$$j_0 = i_0/A_{surf} = Fk_0 C_{ox}^{1-\alpha} C_{red}^{\alpha}$$

Where F is the Faraday constant, A_{surf} the surface area of the catalyst, C_{ox} and C_{red} the concentrations of the redox couple and k_0 measures the kinetic facility of the redox couple of interest. As a benchmark, a typical j_0 value for the HER on a Pt surface is $\sim 10^{-3}$ A cm^{-2}. When j_0 is calculated against the geometrical, projected surface area of the catalytic film (**Figure SI 6a**, $j_{0,geo}$), small variations are observed by changing the porosity of the films through Ar pressure modifications; on the other hand, increasing the MoS_x films thickness leads to a marked $j_{0,geo}$ enhancement, ranging from the smallest value of 10^{-7} A cm^{-2} for the 100 nm films to $\sim 8.5 \cdot 10^{-5}$ A cm^{-2} and $9.5 \cdot 10^{-4}$ A cm^{-2} for the 1 μm- and 2 μm-thick structures respectively. Since the $j_{0,geo}$ parameter is not normalized against the RF_{ec} parameter, i.e. the effective electrochemical surface area, but against the projected geometrical surface area, it can be easily inferred that as the thickness of the MoS_x catalysts is increased, the enhancement of $j_{0,geo}$ is caused by a combined effect of the larger RF_{ec} and easier kinetics of the HER redox couple. Therefore, these $j_{0,geo}$ values suggest the high 'reactivity' and HER activity of the MoS_x catalysts at equilibrium conditions. When the exchange current density is instead normalized to RF_{ec} (**Figure SI 6b**, $j_{0,eff}$) the influence of the porosity features of the MoS_x catalysts can be appreciated: for the various thickness, the MoS_x 5 Pa is the most 'reactive' catalyst because it shows the highest $j_{0,eff}$ values, up to $\sim 8.5 \cdot 10^{-5}$ A cm^{-2} for the 2 μm-thick material. As RF_{ec} increases for the more porous catalysts, instead, the $j_{0,eff}$ values decreases of roughly one order of magnitude and small differences are found for the

MoS$_x$ 10 Pa and MoS$_x$ 30 Pa catalysts. The j$_{0,eff}$ trend with porosity shows how the more compact MoS$_x$ structures are generally characterized by a better activity for the HER reaction at equilibrium, before the porosity and thickness of the nanostructures influence the onset potential and the HER kinetics.

The analysis of the activity descriptors, along with the Tafel slope and η$_{10}$ values, outlines two opposite effects of the catalyst structure on its HER performance. The 100 nm-thick MoS$_x$ structures all show remarkable Tafel slopes of ~35 mV dec^{-1} and are characterized by R$_{CT}$ values of ~8.5 Ω: for these structures, the HER is catalysed with fast kinetics and the Heyrovsky rate determining step is performed faster than the standard, as confirmed by the Tafel slope values below 40 mV dec^{-1}. The low R$_{CT}$ of the 100 nm-thick MoS$_x$ films suggests that, during the Heyrovsky step, the electron transfer rate near HER active sites is efficient, the combination of protons from the electrolyte and electrons from the electrode with a H$_{adsorbed}$ to produce H$_2$ is effective and the reaction kinetics is faster. Despite the remarkable kinetics, the 100 nm-thick films exhibit suboptimal η$_{10}$ values ranging from 175 mV to 189 mV: due to their compact structure and under-developed porosity, they expose a small electrochemical surface area that provides a limited number of active sites in contact with the electrolyte to effectively perform the reaction, as shown by the low RF$_{ec}$ values. Increasing the thickness of the nanostructures to 1 µm is an effective way to increase their electrochemical active area, as confirmed by the higher RF$_{ec}$ values observed, thus decreasing the overpotentials needed to reach -10 mA cm^{-2}: indeed, the η$_{10}$ value ranges from a best of 126 mV to a worst of 157 mV for the 1 µm-thick MoS$_x$ nanostructrures. Furtherly increasing the thickness to 2 µm leads to even higher RF$_{ec}$ values, which almost double with respect to the 1 µm-thick catalysts but still maintain the previous trend with the Ar pressure. However, this increase in RF$_{ec}$ does not find a direct correspondence in the η$_{10}$ values: the three 2

μm-thick morphologies achieve good -10 mA cm^{-2} overpotential values, ranging from 129 mV to 145 mV, but with no evident improvement with respect to the 1 μm-thick films.

Regarding the HER kinetics, the high activity shown by the 100 nm-thick nanostructures and represented by the small Tafel slopes of ~35 mV dec^{-1} is maintained for the MoS$_x$ 5 Pa and MoS$_x$ 10 Pa with a 1 μm thickness. The activity of the more compact structures is confirmed by the j$_{0,eff}$ values, which showed how at equilibrium conditions the more reactive catalysts are the compact, MoS$_x$ 5 Pa ones. Additional increases in surface area of the nanostructures, either by synthesizing more porous morphologies (MoS$_x$ 30 Pa) or 2 μm-thick MoS$_x$ films, worsen instead the HER kinetics as the R$_{CT}$ values are generally higher and the higher Tafel slopes indicate a Volmer-Heyrovsky mechanism performed at a slower rate than the compact films. The worsened kinetics is related to the structure of the more porous and thicker materials. The MoS$_x$ 30 Pa nanostructure, despite its high porosity and electrochemical surface area, is characterized by a high void fraction in the nanostructure connected to its low density. The high background gas pressure diminishes the kinetic energy of the material clusters that build up the MoS$_x$ 30 Pa nanostructure during film growth, leading to weaker interconnecting forces between the clusters and a weaker packing in the nanostructure: this excessive rarefaction of the more porous film results in poor electron transfer properties and slower reaction kinetics. On the other hand, the HER is hampered for the 2 μm-thick MoS$_x$ films by the poorly conductive nature of molybdenum sulfide itself, which combined with the weaker packing of porous PLD nanostructures, ultimately limits the electron transfer rate in the material, limiting the kinetics and the reaction rate.

In this framework, where the variation of morphological parameters has two opposite trends on the catalytic performance, the MoS$_x$ 10 Pa catalyst with 1 μm thickness represents the optimized morphology. It manages to maximize the advantages of the compact MoS$_x$ structure in terms of

HER activity and still exposes a reasonable electrochemical surface area, thus showing the best HER performance not only in terms of a small η_{10} overpotential, whose value of 126 mV is the best found for amorphous, self-supported MoS-based catalyst, but more importantly a remarkable and very efficient reaction kinetics, in terms of both Tafel slope (35.1 mV dec^{-1}) and charge transfer resistance. The small Tafel slope of the compact films is a particularly outstanding result, considering that the majority of MoS-based HER catalysts shows slower HER kinetics with Tafel slope in the range of 40 – 45 mV dec^{-1}, as reported in Table SI 2. The Tafel slope shows the fast reaction rate achieved by the MoS$_x$ films, but combined with the small η_{10} value of the optimized morphology leads to a very efficient operation of the catalyst at high current density, represented by the noteworthy value of 170 mV required to generate a current density of -100 mA cm^{-2}, which is an important criterion for any HER electrocatalyst to be implemented on a large-scale device or on a working electrolyzer.

3.3. Compositional and Structural Analysis of the Pristine and Activated Catalyst

The analysis of the HER activity descriptors as a function of morphological parameters showed that the MoS$_x$ films are intrinsically active for the reaction: all the 100 nm-thick MoS$_x$ materials, where the influence of Ar pressure on porosity is limited and the resulting morphology is almost unvaried, are characterized by small Tafel slope and fast kinetics. Then, the optimization of the electrochemical surface area through thickness and/or porosity tuning of the nanostructure allowed to maximize the η_{10} parameter and maintain a Tafel slope below 40 mV dec^{-1} as in the case of 1 µm-thick MoS$_x$ 5 Pa and MoS$_x$ 10 Pa. Consequently, the fast HER kinetics of the MoS$_x$ catalysts should not stem from a morphological feature but from the material itself, that is, from its elemental composition or structural arrangement. To assess this hypothesis, we analyse both the structure

and the chemical composition of the optimized MoS_x morphology – i.e. the 1 μm-thick MoS_x 10 Pa – before and after the electrochemical 'activation' process. Considering the weak influence of morphology (in terms of both thickness and porosity) on the sulphur-molybdenum coordination, as visualized by the Raman spectra of the different MoS_x materials shown in **Figure SI 7**, and considering the similar effects of the 'activation' process on the composition of the film, as reported in **Figure SI 8**, we can safely extend the considerations we make for the 1 μm-thick MoS_x 10 Pa to all the MoS_x morphologies.

3.3.1. Stoichiometry and Structure for pristine MoS_x

The PLD non-equilibrium synthesis confers to the MoS_x nanostructured films a peculiar microstructural organization, shown in **Figure 5**. The high-resolution SEM micrograph reports more in detail the successive aggregation during PLD synthesis of the materials clusters, with a size of roughly 20 nm, that build up the columnar elements of the MoS_x nanostructure. Further magnification by HRTEM analysis visualizes the nanoscale arrangement of the material, revealing a short-range, ordered structure where, dispersed in an amorphous matrix, embedded crystalline domains are found with a mean size of 8 ± 3 nm and composed of stacks of 3-9 parallel atomic planes with interlayer spacing of 6.8 Å. This distance is consistent with the (002) interlayer distance reported for crystalline MoS_2,[83,84] however we note a larger spacing with respect to the reference, which has been reported in other works and related to lattice expansion in the MoS_2 structure[63] and to an enhanced HER activity thanks to the efficient exposure of sites in a more spaced organization.[28,85,86] In this structure, the ordered nanodomains are characterized by a high density of dislocation defects, indicated in the red circles in **Figure 5b**, and by distorted S-Mo-S layers. The defective nature of the nanodomain is confirmed by the high-angle annular dark-field (HAADF) micrograph in **Figure 5c**: in the image, where the bright spots identify the molybdenum

atoms, the peculiar nanostructure of the PLD films is clearly distinguished. The crystalline nanodomains of the film are organized in multi-layered structures that, differently from crystalline MoS_2, have random orientations and are composed of bent and distorted planes in a wave-like morphology. The bending and distortion of the nanodomains layers induce a strain in the MoS_x planes, which in turn modifies the electronic structure of the material: in the strained region the electronic structure of the molybdenum atoms changes, favouring the adsorption of reactants on the active sites and enhancing the HER.[32,87] This structure is radically different from both layered c-MoS_2 and the polymeric, $[Mo_3S_{13}]^{2-}$ cluster-based organization of a-MoS_x.

Finally, EELS map, obtained by the fitting of the raw data with a procedure outlined in another work[59] (**Figure 5d**) visualizes the composition of the pristine material which is characterized by an anisotropic elemental distribution, with regions enriched with either Mo or S, as a consequence of the PLD synthesis process. Despite the anisotropic stoichiometry, the Mo:S ratio extrapolated from the area-averaged EELS spectra reported in **Figure SI 9** is 1:2.4, which is between the 1:2 ratio of c-MoS_2 and the typical 1:3 ratio reported for amorphous MoS_x.[17] Interestingly, the Mo:S ratio for the pristine MoS_x changes with the distance from the particles surface: **Figure SI 10** shows how the Mo:S ratio ranges from 1:3.89 for the particle surface to 1:1.77 for a distance of roughly 16 nm from the surface, further confirming the inhomogeneous composition of the pristine catalyst and an evident excess of sulfur on the surface of the material.

Due to its microstructure, characterized by ordered, highly-defective nanodomains dispersed in an amorphous matrix, the pristine MoS_x is X-ray amorphous, since the characteristic c-MoS_2 diffraction peaks do not appear in the grazing incidence X-ray diffraction (GI-XRD) spectrum of the pristine film, shown in blue trace in **Figure 6a**. Other features with low intensity are however registered at 40.5°, 58.6° and 73.7°. These features correspond respectively to the (110), (200) and

(112) peaks of metallic molybdenum, as confirmed by the reference XRD pattern. The presence of metallic molybdenum in the MoS_x nanostructure is directly related to the employed synthesis method:[88,89] during ablation the chalcogen is preferentially ablated from the c-MoS_2 target, whose surface depleted in sulfur becomes metallized. When a successive laser pulse hits the target, metallic Mo nanoparticles are ablated from the target occasionally and land on the nanostructures growing on the substrate, accounting for the Mo peaks that can be seen in the diffractogram of the pristine MoS_x. While the nanodomains composed of the distorted S-Mo-S planes are not registered by GI-XRD, their fingerprint is effectively captured by low-frequency Raman spectroscopy: the map-mediated spectrum of the pristine MoS_x (blue trace in **Figure 6b**) is characterized by a distribution of features in the Stokes and anti-Stokes regions, respectively in the 8 cm^{-1}–23 cm^{-1} and -18 cm^{-1}– -5 cm^{-1} ranges. While attribution of these features is not trivial, since in the literature reports solely about crystalline molybdenum sulfides are found, we ascribe them to the breathing modes of the bent, layered nanocrystalline domains, because the position of the features well matches the ones reported for crystalline molybdenum sulfide inter-layer breathing modes.[90,91] Since the layered domains are characterized by defects and are dispersed in an amorphous matrix, their vibration does not correspond to single peaks in the low-frequency Raman spectrum but, instead, to broader features. The coordination between metal, chalcogen and other elements in the material is then visualized by (standard) high-frequency Raman spectroscopy, with the spectrum of the pristine MoS_x presented in blue trace in **Figure 6c**. The pristine MoS_x catalyst displays the characteristic features of amorphous molybdenum sulfide films reported in the literature.[49,51,57] The band registered at 230 cm^{-1} is attributed to the vibration of the Mo-Mo bond ν(Mo-Mo), while the ones found at 289 cm^{-1}, 328 cm^{-1}, 352 cm^{-1} and 380 cm^{-1} are associated to the vibration of the molybdenum sulfide bonds ν(Mo-S). The feature at 455 cm^{-1} is ascribed to the ν(Mo_3-μS)

vibrational mode, i.e. the vibration of an S atom bridging three Mo atoms in a a-MoS$_x$ cluster organization,[57] while the two features at 523 cm^{-1} and 554 cm^{-1} stem from the disulfide vibrations, respectively the bridging/shared disulfide v(S-S)$_{br/sh}$ and the terminal disulfide v(S-S)$_t$. In the high Raman shifts region, between 750 cm^{-1} and 1000 cm^{-1}, a broad band with weak intensity is registered, related to surface stoichiometric MoO$_3$ formed upon manipulation of the material in atmosphere. The STEM-EDX maps acquired for the pristine MoS$_x$ and shown in **Figure 6d** and **Figure 6f** confirm the presence of sulfur in the material and of surface oxygen, in accordance with the previous data.

Lastly, X-Ray photoelectron spectroscopy (XPS) is employed to probe the surface of the MoS$_x$ catalyst. The data collected for the pristine MoS$_x$, in the energy region typical for S 2p and Mo 3d are shown in **Figure 7a** and **Figure 7b** along with the fitted spectra. In the S 2p region two distinct sulfur species are present, which give rise to two doubles whose S 2p$_{3/2}$ components are centered at 162.1±0.3 eV and 163.4±0.3 eV, respectively. The doublet at lower energies is ascribed to terminal S$_2^{2-}$ and unsaturated S^{2-}, while the doublet at higher energies is ascribed to apical S^{2-} and bridging S$_2^{2-}$, in agreement with previous literature works on amorphous molybdenum sulfide catalysts.[57,75,92] The presence of these two S species is also reflected in the spectrum of the Mo 3d region, where the S 2s contributions of terminal S$_2^{2-}$/unsaturated S^{2-} (peak at 226.4 eV) and of apical S^{2-}/bridging S$_2^{2-}$ (peak at 227.4 eV) are present and partially overlapped with the Mo signals. The Mo signal itself is deconvoluted into two doublets. The first one present a high-intensity Mo 3d$_{5/2}$ component centered at 229.2±0.3 eV and is indicative of molybdenum atoms with a 4$^+$ oxidation state, ascribed to the Mo^{IV} centers of amorphous MoS$_x$ materials.[75,92,93] The second doublet, with significantly lower intensity, has a 3d 5/2 component centered at a 232.6±0.3 eV and can be ascribed to Mo^{VI} centers, likely due to the presence of superficial MoO$_3$ in the pristine

material after its manipulation in atmosphere.[52,75,92,94–96] These molybdenum atoms with a 6^+ oxidation state only account for approximately 8% of the initial molybdenum content in the pristine nanostructured material. No evidence of metallic Mo – observed via XRD – has been recorded with the XPS analysis, suggesting that the metallic species are located beneath the probing depth of few nanometers typical of XPS measurements. Overall, the surface Mo:S atomic ratio for the pristine MoS_x nanostructures is 21:79, corresponding to a $MoS_{3.8}$ stoichiometry with an evident excess of sulfur with respect to the MoS_3 stoichiometry reported for many a-MoS_x catalysts, related to the preferential chalcogen sputtering from the MoS_2 target during ablation and the segregation between molybdenum and sulfur.

3.3.2. Stoichiometry and Structure for activated MoS_x

While the pristine MoS_x is characterized by a highly defective and nanocrystalline structure, the actual catalytic material (activated MoS_x) is generated *in-situ* during the electrochemical 'activation' process, detailed in **Section 2**, through a series of stoichiometric and structural modifications that are visualized in **Figures 6** and **Figure 7**. Firstly, the process irreversibly alters the structure of the activated MoS_x: differently from its pristine state, the activated MoS_x undergoes a marked amorphization upon the process with a loss of order. Indeed, in the HAADF micrographs and SAED (Selected Area Electron Diffraction) pattern in **Figure SI 11** and **Figure SI 12b** the bent, layered nanodomains that characterized the structure of the pristine MoS_x are not present and no short-range, periodic structure can be distinguished for the activated material. This phenomenon has been observed in other works, where the interaction of amorphous molybdenum sulfide with acidic electrolyte triggers a structural rearrangement in the catalyst, for example by an amorphization/crystallization process[97] or by reduction of defects of the molecular arrangement of the material.[57] Accordingly, the GI-XRD diffractogram of the activated MoS_x (red trace in **Figure**

6a) shows changes with respect to the pristine state, with the (200) and (112) molybdenum peaks disappearing completely and the (110) peak significantly decreasing in intensity. The loss of order and amorphization of the activated MoS_x are also reflected in the low-frequency Raman spectrum (red trace in **Figure 6b**), where the inter-layer breathing features previously found for the pristine material disappear, shifting to lower numbers and overlapping with the signal at 0 cm^{-1} caused by the Raman laser reflection. In analogy to crystalline MoS_2, where the shift to lower wavenumbers for the inter-layer breathing modes is related to a higher number of layers vibrating in the structure,[90,91] we ascribe this shift of the inter-layer breathing modes to a structure that, due to its amorphization, loses its ordered plane stacking through agglomeration of the nanocrystalline domains in bigger and more disordered structures, in accordance with the HAADF micrographs reported in **Figure SI 11**. Along with the change in structure, the 'activation' process modifies the compositional properties of the MoS_x, in analogy to other amorphous molybdenum sulfide catalysts reported in literature.[56,57,92] The Raman bands associated to the molybdenum sulfide bonds ν(Mo-S) in the 280 cm^{-1} –380 cm^{-1} region collapse into one broader feature centered at 329 cm^{-1}. A shift towards lower wavenumber is observed for the ν(Mo$_3$-μS) feature – from 455 cm^{-1} to 438 cm^{-1} – along with the disappearance of the two ν(S-S) features at 523 cm^{-1} and 554 cm^{-1}. The disappearance of the S-S vibrational bands and the shift of the ν(Mo$_3$-μS) feature are associated to the removal of terminal disulfide ligands in the material, caused by the release of excess sulfur during the 'activation' process, and to a subsequent change in the ligands geometry in the material after activation, in accordance to other reports found in the literature.[57,58] Moreover, new features at 201 cm^{-1}, 427 cm^{-1} and 484 cm^{-1} are observed. While in this region different signals from MoS-, MoO- and MoOS-based compounds overlap, making a univocal identification for these bands difficult, the incorporation of oxygen in the structure triggered during the 'activation' procedure

allows us to ascribe these features to the vibrations of bridging sulfur – ν(Mo-S-Mo) at 427 cm^{-1} and 484 cm^{-1} –[52,98] and oxygen – ν(Mo-O-Mo) at 201 cm^{-1} –[44] in reduced molybdenum oxide/oxysulfide species. An evident modification affects the Raman signature of the activated material in the high shifts region. There, three main features (**Figure SI 13**) appear at approximately 770 cm^{-1}, 857 cm^{-1} and 930 cm^{-1}: similarly to the previous vibrational bands, these features can be ascribed to different molybdenum compounds containing oxygen and sulfur and therefore a univocal identification is not possible. However, due to the incorporation of oxygen in the activated MoS$_x$, we ascribe these vibrations to oxygen-molybdenum bonds with different coordination (770 cm^{-1} for ν(Mo$_3$-O), 857 cm^{-1} for ν(Mo$_2$-O), 930 cm^{-1} for ν(Mo=O)) in amorphous molybdenum oxides[94,96] or oxysulfide species.[98] The presence of vibrational bands ascribed to Mo-O$_x$ bonds, along with the increase in O percentage and the decrease in S percentage shown by STEM-EDX maps for activated MoS$_x$ in **Figure 6e** and **Figure 6g,** confirm that during the 'activation' process the MoS$_x$ catalyst incorporates oxygen. The excess sulfur of the MoS$_{3.8}$ stoichiometry is released from the surface of the material and oxygen is incorporated in the structure with different coordination, creating oxide/oxysulfide phases through the amorphization of the material. The activated material is characterized a compresence of both amorphous molybdenum sulfide and non-stoichiometric molybdenum oxide/oxysulfide phases (stoichiometric MoO$_3$ is soluble in strong acids[92,99] and any formed MoO$_3$ is dissolved during electrochemical activity), which is able to enhance the HER performance of the material: indeed, in accordance with a number of previous works, [43–45,47,100] incorporating oxygen in a molybdenum sulfide structure increases the electrical conductivity of the material thus enabling a faster HER kinetics and a better catalytic performance. The compositional modifications triggered by the 'activation' process are particularly evident on the catalyst surface, as shown by the S 2p and Mo

3d regions XPS spectra in **Figure 7c** and **Figure 7d**. For the sulfur region, the intensity of the apical S^{2-}/bridging S_2^{2-} doublet at higher energy strongly decreases, almost disappearing. On the other hand, the lower energy doublet ascribed to the terminal S_2^{2-}/unsaturated S^{2-} is still present and its intensity less affected by the electrochemical testing. The intensity decrease for the apical S^{2-}/bridging S_2^{2-} doublet further confirms the release of sulfur from the material structure upon electrochemical testing, as was suggested by Raman spectroscopy and electrochemical analysis. A low-intensity doublet with its S $2p_{3/2}$ component centered at 168.5 ± 0.3 eV is also registered, related to sulfur in a 6^+ oxidation state and assigned to SO_4^{2-} groups arising for the surface oxidation occurring upon electrochemical testing, as similarly reported in previous works.[101,102] Concerning the Mo 3d region, the apical S^{2-}/bridging S_2^{2-} doublet at 227 eV related to decreases concordantly to its S 2p counterpart, while the terminal S_2^{2-}/unsaturated S^{2-} doublet at 226 eV is marginally affected. The doublet centered at 229.2 eV ascribed to Mo^{IV} compounds of the amorphous MoS_x phase severely decreases in intensity and an additional Mo 3d doublet appears close-by, with its Mo $3d_{5/2}$ component centered at 229.7 ± 0.3 eV. This doublet too is ascribed to Mo^{IV} compounds, but slightly shifted to higher binding energy values. The attribution of the new doublet to a specific Mo^{IV} compound is not trivial: XPS elemental analysis on porous samples with a complex geometry requires advanced modelling and strong assumptions on the spatial distribution of the elements. However, given the absence of other elements at the sample surface, we restrict the attribution of this doublet to a sub-stoichiometric molybdenum oxide MoO_2 phase[43,44,94,103] or to a combined oxysulfide phase with stoichiometry $Mo^{IV}O_yS_z$. The oxidation of the sample is also reflected by the increased intensity of the Mo^{VI} doublet related to MoO_3 compounds, accounting for almost 15% of the total Mo content for the activated material. In addition, the surface Mo:S atomic ratio for the activated material becomes 35:65, corresponding

to a $MoS_{1.9}$ stoichiometry, as a further proof of the assumed loss of excess sulfur during the electrochemical testing. The presence of surface sub-stoichiometric oxide phases in the activated MoS_x catalyst is related to an enhanced catalytic activity through the increase of the electrical conductivity of the material and a faster charge transfer during HER, in accordance with previous reports where the incorporation of oxygen in a molybdenum sulfide catalyst, either by doping or by the compresence of a MoO_2 phase near the catalytically active MoS_2 phase, improved the catalytic activity of the material.[43,44,100]

3.4. High current stability and comparison

A paramount requirement for any nonprecious HER electrocatalyst in a working electrolyzer is the ability to operate efficiently and continuously at high current density, with sustained hydrogen gas generation. Indeed, typical operative current densities for these devices range from 500 mA cm^{-2} for alkaline electrolyzers[104] to 1 A cm^{-2} and more for PEM electrolyzers.[105] In this regard, the optimized MoS_x 10 Pa catalyst with 1 μm thickness is characterized by an outstanding HER performance in these operating conditions, even if this working regime is tested for our catalyst in an experimental setup – a three-electrode cell with liquid electrolyte – with a markedly different environment from what is found in a real-life PEM electrolyzer.

The first parameter describing the high-current operation of the catalyst is the η_{100} overpotential, which was previously introduced in **Section 3.2**. The optimized MoS_x catalyst is characterized by a η_{100} of 170 mV, as extrapolated from the iR-corrected LSV curves, which stands as one of the best values achieved by MoS-based catalyst irrespective or their nature (crystalline or amorphous). A detailed comparison between the PLD-synthesized MoS_x film and several other catalyst of the molybdenum sulfide family is reported in **Table SI 2**, where the η_{100} and the Tafel slope are employed as main figures of merit, and a graphical comparison of the HER catalytic performance

of the optimized MoS_x catalyst and of other selected MoS-based catalyst is shown in **Figure 8a**. In this comparison plot, where only MoS-based catalyst that reach a current density of at least - 100 mA cm^{-2} in an iR-corrected LSV measurement are reported, the remarkable performance in terms of both small η_{100} of 170 mV and fast HER kinetics of the optimized MoS_x can be appreciated, outperforming the majority of MoS-based catalysts, whether crystalline or amorphous. It is important to highlight how the best-performing MoS-based catalysts found in the literature and reported in the comparison table employ a support material – e.g. a porous nickel foam[106] or carbon black[63] – on top of which the catalytic material itself is deposited. By recalling the definition of η_{100}, that is the overpotential required to generate a geometric current density of -100 mA cm^{-2}, it can be seen how the synthesis of a support structure with a 3D controlled morphology is an efficient method for increasing the electrochemical roughness factor of the catalytic architecture, and consequently to improve the η_{100} parameter through an increase of the electrochemically active surface area. Despite the remarkable η_{100} value achieved by these catalysts, their Tafel slope lies in the typical range of MoS-based materials, between 40 mV dec^{-1} and 50 mV dec^{-1}: while their electrochemical surface area is maximized, the reaction kinetics, which depends on the intrinsic activity of the catalytic material, is not fully optimized. On the other hand, the PLD-synthesized MoS_x catalyst with the optimized morphology achieves a η_{100} of 170 mV without any support structure, thanks to the coupled beneficial effect of a good onset potential (η_{10}=126 mV) and a very efficient HER kinetics, represented by the 35.1 mV dec^{-1} Tafel slope. This Tafel slope value, which is achieved not only by the optimized MoS_x but also by the more compact PLD-synthesized films, is smaller than the usually reported range for MoS-based catalysts, where the limited electrical conductivity of the material itself hinders the HER kinetics. For the PLD-synthesized MoS_x catalysts instead, the incorporation of oxygen in the material to

form sub-stoichiometric oxide/oxysulfide phases with high electrical conductivity enhances the electron transfer rate to the HER active sites during the reaction resulting in the optimal Tafel slope values. Similarly to our MoS_x catalyst, the positive effect on the HER kinetics of a higher electrical conductivity, due to the presence of elements or dopants that improve the electron transfer, has been reported in other literature works.[19,44]

Lastly, a turnover frequency (TOF) comparison is carried out between the optimized MoS_x catalytic architecture and the other MoS-based catalysts grouped in **Table SI 2**. TOF calculation is performed employing the method outlined by Jaramillo's group[73] (detailed in the **Supplementary Information**) and the result is plotted in **Figure SI 14**. While a defined standard for TOF calculation for MoS-based catalysts is still lacking, a qualitative comparison can still be performed. For a 100 mV overpotential (current density of 1.96 mA cm^{-2}), the optimized MoS_x 10 Pa is characterized by a TOF ranging from 0.06 to 0.16 H_2 s^{-1} per site according to the simplification employed for surface active sites estimation. These values are in the same range of other MoS-based materials with crystalline nature at the same applied overpotentials, e.g. a sulfur-depleted 1T-MoS_2 catalyst with a TOF of 0.15 H_2 s^{-1} per site[107] or a Zn-doped c-MoS_2 with per-site TOF of 0.67 H_2 s^{-1},[42] and significantly higher than amorphous molybdenum sulfide materials that reach such TOF values at overpotentials equal to or higher than 150 mV (**Table SI 2**). Moreover, at an applied overpotential of 170 mV (current density of 100 mA cm^{-2}), the per-site TOF markedly increases to a 1.2-3.5 H_2 s^{-1}, outperforming in one order of magnitude many MoS-based materials and standing among the most active catalysts of the family, thus further confirming the remarkable activity of the optimized MoS_x architecture: indeed, per-site TOFs range at higher applied overpotentials usually lie in a range from 1.4 H_2 s^{-1} [63]-1.86 H_2 s^{-1} [107] at 150 mV to 0.4 H_2 s^{-1} [19]-3.5 H_2 s^{-1} [108]-20.6 H_2 s^{-1} [84] at 200 mV.

In addition to the HER performance, the MoS_x catalyst shows also a remarkable stability during continuous operation, another important parameter for an HER electrocatalyst operating in a full electrolyzer device, as demonstrated through chronopotentiostatic measurements. The MoS_x catalyst is characterized by a remarkable electrochemical stability over more than 100 hours of uninterrupted operation at an applied current density of -100 mA cm^{-2}, with a required (non iR-corrected) overpotential of ~400 mV to sustain such current density (**Figure SI 15a**). Benchmarking the obtained value against a Pt mesh catalyst reference in the same experimental setup reveals the good high-current performance of the MoS_x catalyst, since the Pt standard requires an average overpotential of ~198 mV to sustain the same current density, just half of the overpotential required by the MoS_x catalyst, as visualized in **Figure SI 15b.** When the applied current density is increased of one order of magnitude to -1 A cm^{-2}, the remarkable performance of the optimized MoS_x is even more evident: not only the material still shows an excellent electrochemical stability over 25 hours of continuous operation, requiring an average overpotential of 851 mV at that applied current density as visualized in **Figure SI 15c**, but more importantly when its performance is compared against the Pt mesh reference at -1 A cm-2 in the same setup (chronoamperometry shown in **Figure SI 15d**), the required overpotential of the optimized MoS_x is roughly the same of the Pt reference. Indeed, the performance comparison shown in **Figure 8b** visualizes how in a high-current-density operating conditions the catalytic behavior of the optimized MoS_x is very similar to Pt mesh reference, which requires an average overpotential of 953 mV to sustain -1 A cm^{-2} for 6 hours.

The operation at such current density and the long-term stability of the optimized MoS_x nanostructure, with particular attention to the 100 hour-stability at -100 mA cm^{-2} and the Pt mesh-like performance at -1 A cm^{-2}, are an unprecedented result for an amorphous MoS-based material,

considering that to the best of our knowledge no results are found for amorphous MoS-based catalysts with such long-lasting stability at such applied current density and may pave the way for a new design of a-MoS$_x$ catalysts to be integrated in working electrolytic devices.

4. Conclusions

In our work, we exploited the non-equilibrium characteristics of Pulsed Laser Deposition to grow nanostructured, molybdenum sulfide-based HER catalysts characterized by a nanocrystalline, defective organization at the nanometric scale where, dispersed in an amorphous molybdenum sulfide matrix, nanocrystallites are embedded composed of bent and distorted molybdenum disulfide layers. The peculiar atomic organization of the PLD-grown MoS$_x$ catalysts originates from the controlled condensation and nucleation of nanoparticles and aggregates of material in the plasma plume, generated by the laser ablation of a c-MoS$_2$ target, and by the reciprocal interaction between the ions, atoms and particles that constitute the different plasma components, e.g. the interaction between the highly-energetic 'rebound' particles and the slower, heavier aggregates ablated from the target in the 'tail' component. Along with their interaction in the plasma plume, the background gas pressure affects the kinetic energy of the particles during deposition. Depending on their final energy as they impinge the substrates, the sequential landing on the substrates of the particles grows MoS$_x$ films with distinct morphological features, ranging from compact films to porous hierarchical nanostructures. The nanocrystalline structure of the pristine MoS$_x$ catalysts is confirmed by low- and high frequency Raman spectroscopy, which register the interlayer vibration of the S-Mo-S distorted layer in the nano-crystallites and the Mo-S vibrational bonds of a-MoS$_x$ materials respectively. To improve the electron transfer rate of the MoS$_x$ catalyst, we incorporate oxygen in the material during the electrochemical 'activation' process, where concomitantly to the release of excess sulfur from the surface oxygen is

incorporated to form sub-stoichiometric oxide/oxysulfide phases, confirmed by Raman and XPS spectra, with enhanced electrical conductivity that promote a fast hydrogen evolution kinetics.

The PLD-grown, oxygen-incorporated MoS_x catalysts exhibit a remarkable catalytic activity, as shown by the Tafel slope of $\sim$35 mV dec^{-1} or the small charge transfer resistance of the 100 nm-thick films which are related to a very fast HER kinetics. By tuning, during PLD synthesis, morphological parameters like porosity, nanostructuration and thickness of the MoS_x catalysts, we identify two opposite effects of morphology on HER performance: thicker and more porous films increase the exposed surface area available for the reaction, thus decreasing the overpotential required for the reaction with respect to the 100 nm-thick films, but the rarefaction effect of the more porous MoS_x nanostructures hampers the electron transfer rate resulting in sluggish reaction kinetics and worse Tafel slope. The best trade-off between the fast kinetics of thin, compact structures and the low onset potential of thick, porous ones is represented by the MoS_x 10 Pa with a total thickness of 1 μm. This optimized architecture currently stands as the state-of-the-art for MoS-based amorphous self-supported electrocatalyst, thanks to its remarkable electrochemical performance in terms of both onset potential (η_{10} = 126 mV, η_{100} = 170 mV) and kinetics (Tafel slope = 35.1 mV dec^{-1}). With its optimized charge transport properties, our architecture outperforms even several supported and/or crystalline MoS-based catalysts reported in literature, surpassing the renowned advantage provided by a supporting conductive scaffold or by an ordered, crystalline structure. Finally, the optimized MoS_x catalyst achieves an unprecedented stability result among amorphous MoS-based materials, with a 100-hour stability after continuous operation at an applied current density of -100 mA cm^{-2} and a 25-hour stability at -1 A cm^{-2}, representing a remarkable result towards the implementation of highly active, non-crystalline MoS-based systems in real-world electrolyzers.
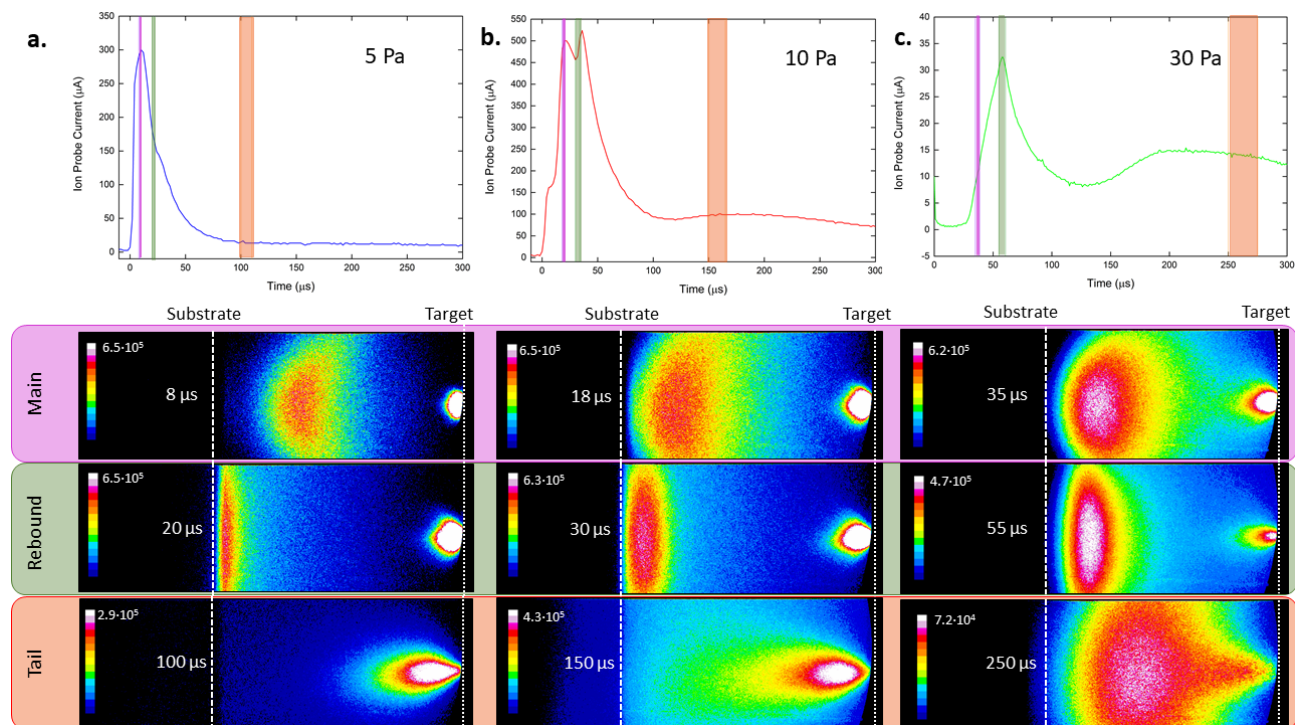
Figures

Figure 1. – a-c. Ion probe plots (upper part) and corresponding ICCD images (lower part) for PLD synthesis of MoS_x nanostructures with different Ar pressure. Highlighted are three main components of the plasma plume: violet shows the main component, green the rebound component on the substrate, red highlights the second emission of the heavier nanoparticles ('tail' component).
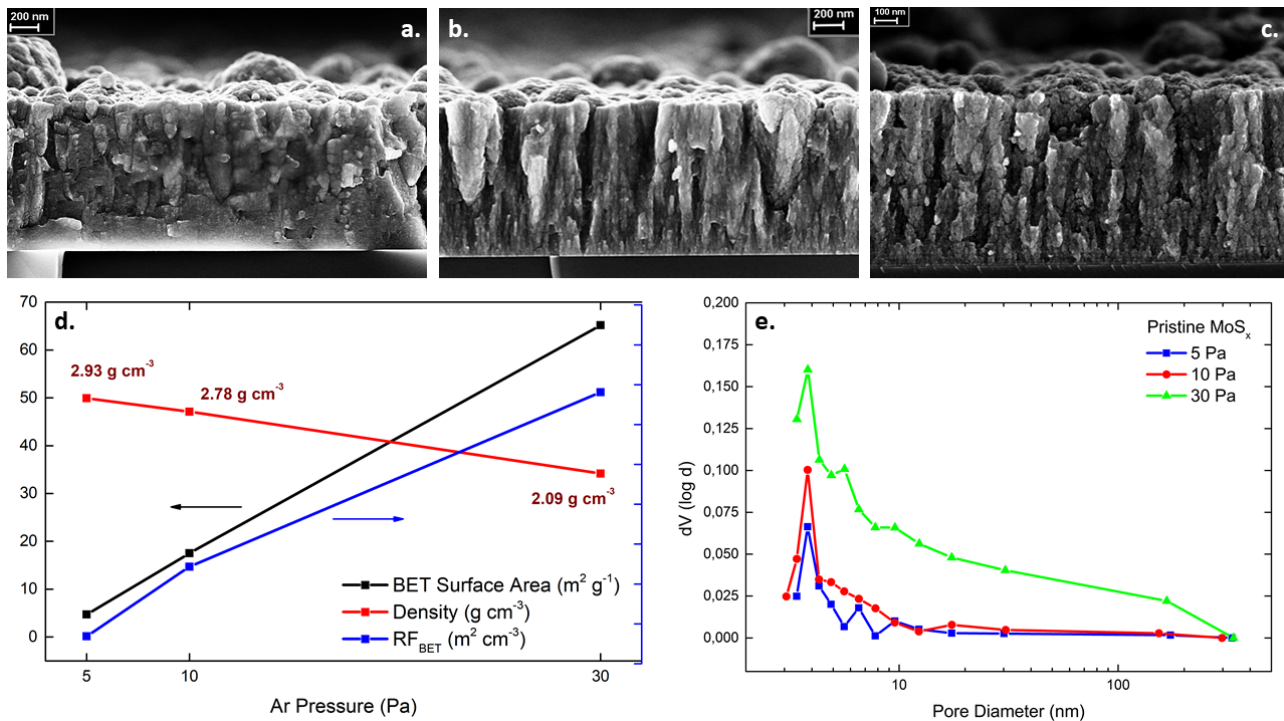
Figure 2. a-c. SEM cross-sectional micrographs showing the morphology of the as-deposited PLD nanostructures with a representative thickness of 1 μm. a. MoS_x 5 Pa, b. MoS_x 10 Pa, c. MoS_x 30 Pa. d. Morphological features – BET surface area, density and BET-derived roughness factor and e. BJH pore size distribution for the pristine MoS_x nanostructured films.
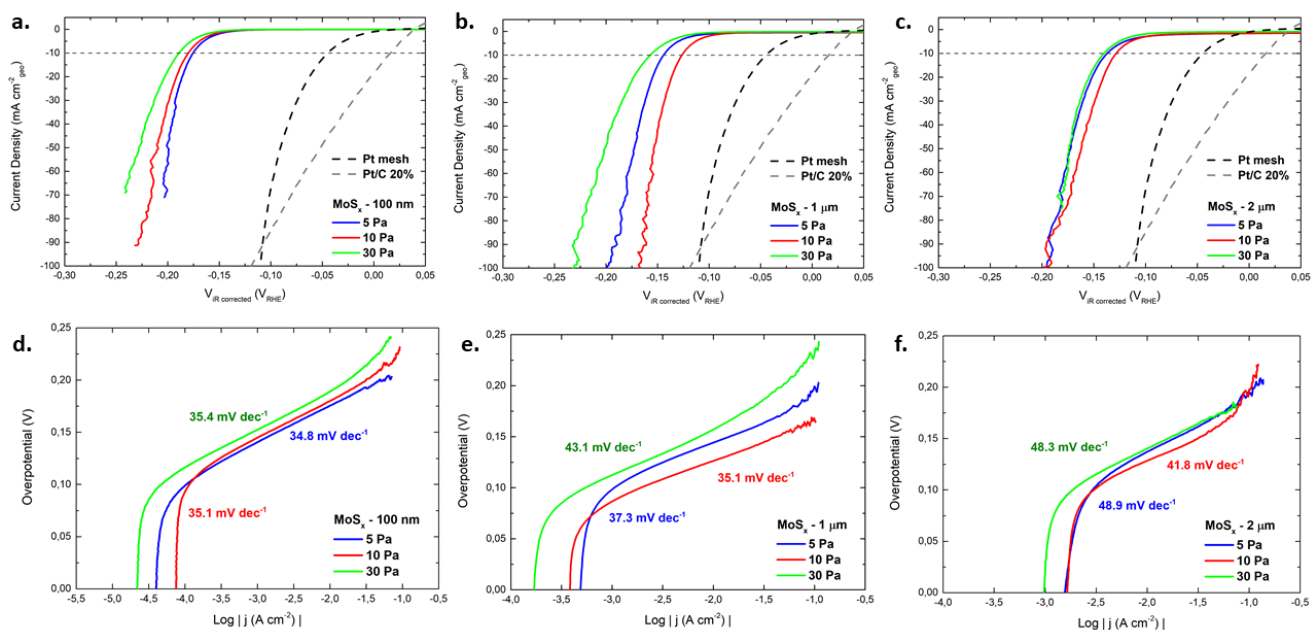
Figure 3. Electrochemical performance of MoS$_x$ nanostructures for the hydrogen evolution reaction. a-c. iR-corrected linear sweep voltammograms, d-f. corresponding Tafel plots. a. and d. 100 nm-thick MoS$_x$, b. and e. 1 µm-thick MoS$_x$, c. and f. 2 µm-thick MoS$_x$. In the LSV plots, the black dashed line corresponds to a laboratory Pt mesh reference while the grey dashed line represents a commercial Pt/C 20% (Pt loading 0.2 mg cm^{-2}) reference.
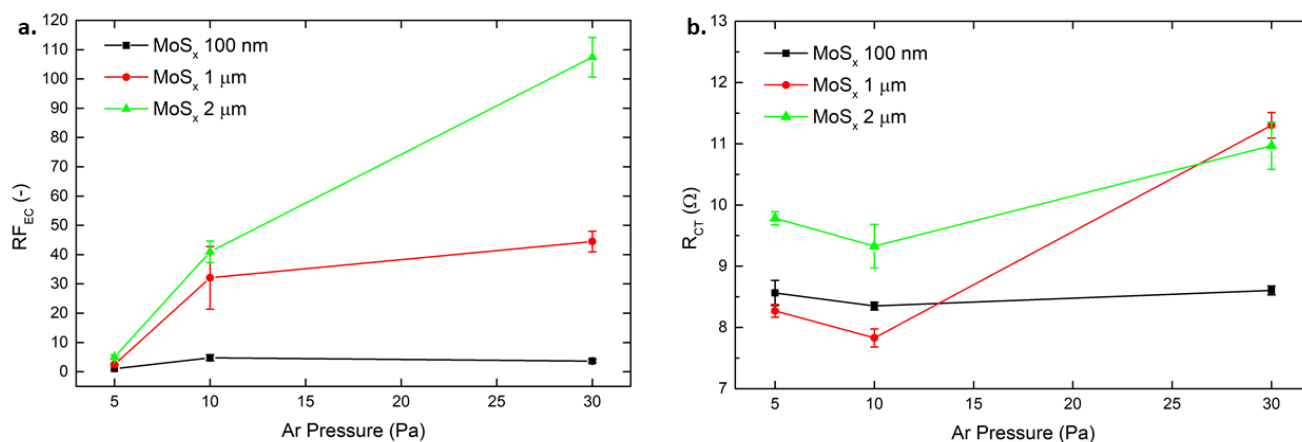
Figure 4. Electrochemical figures of merit for MoS$_x$ nanostructures with different thickness and morphology (Ar pressure). a. shows the increase of electrochemical roughness factor – i.e. electrochemical surface area – with increasing porosity and thickness of the nanostructures, while b. shows the effect of morphological features on the charge transfer resistance.
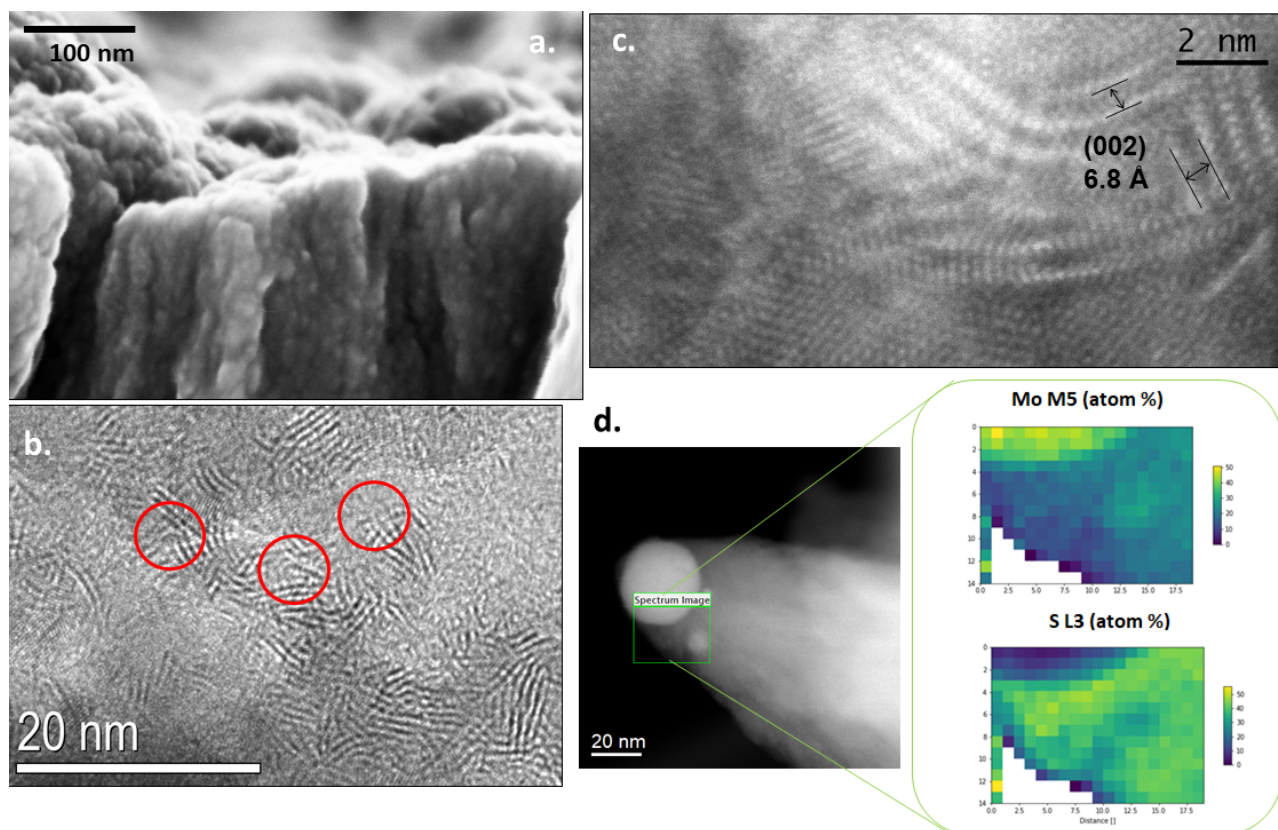
Figure 5. Organization at the nanoscale of the as-synthesized MoS_x catalyst: a. close-up SEM cross section image of the nanotrees, b-c. nanocrystalline structure of the material, with enlarged interlayer spacing, defects (red circles in b), and bent and distorted S-Mo-S planes. d. atomic distribution derived from EELS map acquired in the green area for a representative portion of the pristine MoS_x catalyst.
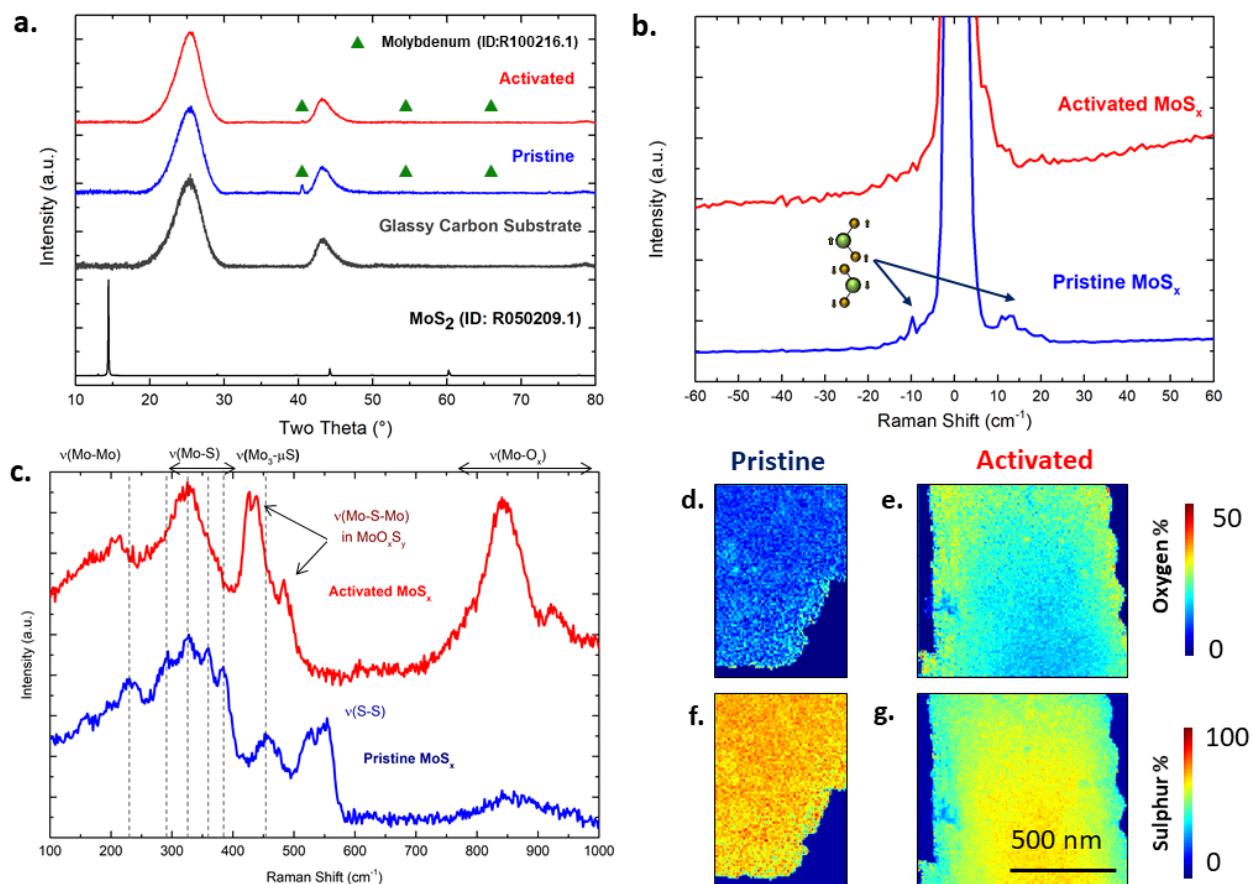
Figure 6. Composition of the pristine and activated MoS_x catalyst. a. XRD pattern, b. low frequency and c. high frequency Raman spectroscopy. Blue trace indicates the pristine material, while the red trace the activated catalyst. In the X-Ray pattern, molybdenum, molybdenum sulfide and glassy carbon reference are reported. d-g. show qualitative STEM-EDX maps for oxygen and sulfur in the pristine and activated material, to highlight the change in composition upon electrochemical activation. d. oxygen percentage and f. sulfur percentage for pristine MoS_x, e. oxygen and g. sulfur percentage for activated MoS_x.
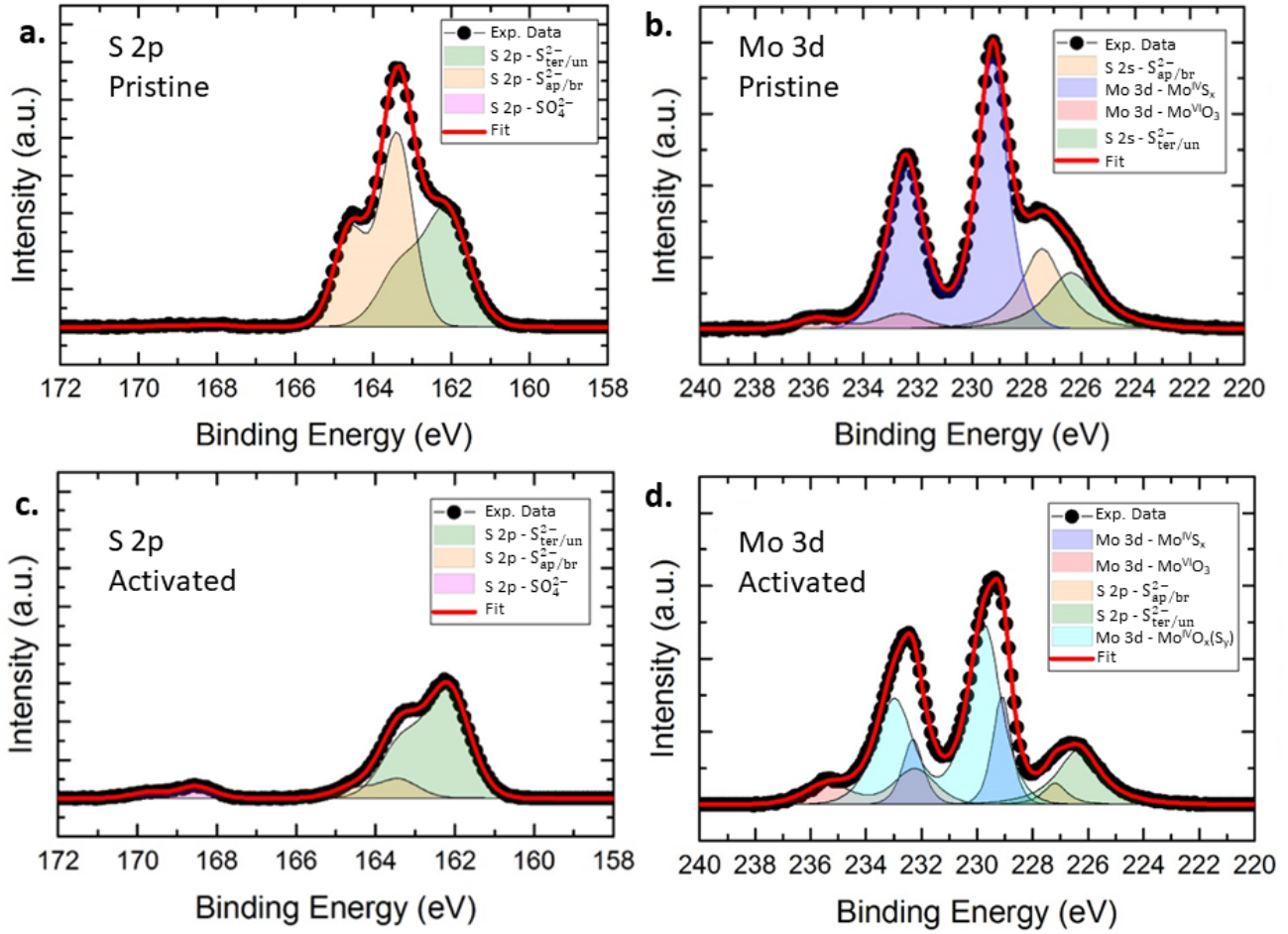
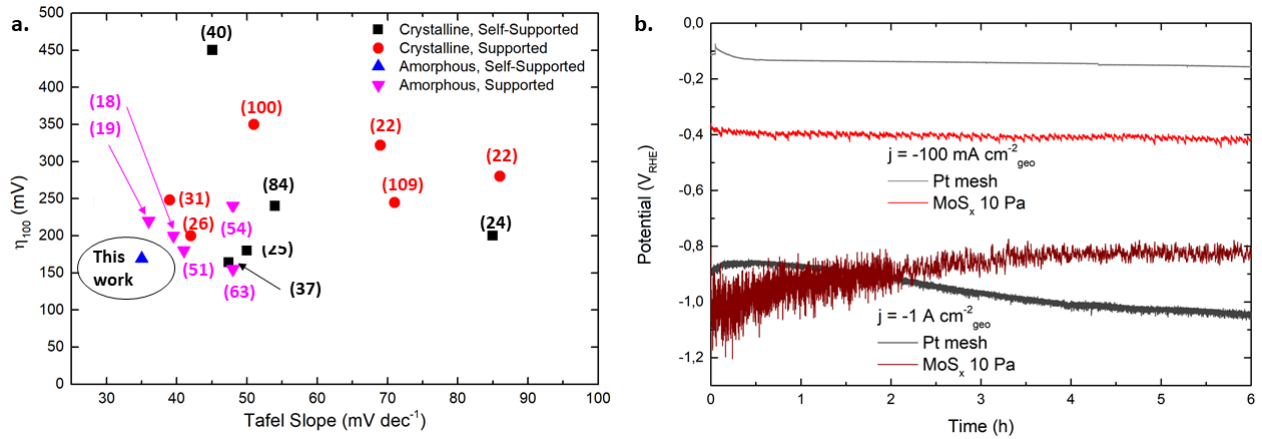**Figure 7.** XPS spectra for a-b. pristine and c-d. activated MoS_x catalyst, in the S 2p and Mo 3d regions.

Figure 8. a. Comparison based on Tafel slope and η_{100} values between the PLD-synthesized MoS_x material and other catalysts of the MoS family, divided among crystalline self-supported MoS_2,[25,26,37,40,84] crystalline supported MoS_2,[23,27,31,100,109] and amorphous supported a-MoS_x.[18,19,51,54,63] b. Chronopotentiometry at applied current densities of -100 mA cm^{-2} of -1 A cm^{-2} for the optimized 1 µm-thick MoS_x 10 Pa catalyst, benchmarked against a Pt mesh reference. The potentials are reported without iR correction.

Supporting Information

Supporting information for the present manuscript are provided in a separate file. The SI contains additional data on the electrochemical 'activation' process, fitting of the Mo-Ox Raman bands in the activated catalyst, details on the RFec and TOF calculations, a counter electrode comparison between Pt and C, HIM-SIMS analysis and a comparison table between representative MoS-based HER electrocatalysts. The following files are available free of charge.

Author Information

*Corresponding author, to whom correspondence should be addressed. Contact address: fabio.difonzo@iit.it

§ Present affiliation for A. Perego: National Fuels Cell Research Center, University of California Irvine, Irvine, CA 92617, USA

Author Contributions

The manuscript was written through contributions of all authors. All authors have given approval to the final version of the manuscript. ‡These authors contributed equally. (match statement to author names with a symbol)

References

(1)   de Levie, R. The Electrolysis of Water. *J. Electroanal. Chem.* **1999**, *44* (2), 120–125. https://doi.org/10.1007/s11124-008-2002-x.

(2)   Anantharaj, S.; Ede, S. R.; Sakthikumar, K.; Karthick, K.; Mishra, S.; Kundu, S. Recent Trends and Perspectives in Electrochemical Water Splitting with an Emphasis on Sulfide, Selenide, and Phosphide Catalysts of Fe, Co, and Ni: A Review. *ACS Catal.* **2016**, *6* (12), 8069–8097. https://doi.org/10.1021/acscatal.6b02479.

(3)   Barreto, L.; Makihira, A.; Riahi, K. The Hydrogen Economy in the 21st Century: A Sustainable Development Scenario. *Int. J. Hydrogen Energy* **2003**, *28* (3), 267–284. https://doi.org/10.1016/S0360-3199(02)00074-5.

(4)   Marbán, G.; Valdés-Solís, T. Towards the Hydrogen Economy? *Int. J. Hydrogen Energy* **2007**, *32* (12), 1625–1637. https://doi.org/10.1016/j.ijhydene.2006.12.017.

(5)   Walter, M. G.; Warren, E. L.; McKone, J. R.; Boettcher, S. W.; Mi, Q.; Santori, E. A.; Lewis, N. S. Solar Water Splitting Cells. *Chem. Rev.* **2010**, *110* (11), 6446–6473. https://doi.org/10.1021/cr1002326.

(6)   Carmo, M.; Fritz, D. L.; Mergel, J.; Stolten, D. A Comprehensive Review on PEM Water Electrolysis. *Int. J. Hydrogen Energy* **2013**, *38* (12), 4901–4934. https://doi.org/10.1016/j.ijhydene.2013.01.151.

(7)   Zou, X.; Zhang, Y. Noble Metal-Free Hydrogen Evolution Catalysts for Water Splitting. *Chem. Soc. Rev.* **2015**, *44*, 5148–5180. https://doi.org/10.1039/C4CS00448E.

(8)   Roger, I.; Shipman, M. A.; Symes, M. D. Earth-Abundant Catalysts for Electrochemical and Photoelectrochemical Water Splitting. *Nature Reviews Chemistry*. Macmillan Publishers Limited 2017. https://doi.org/10.1109/TDEI.2009.5211872.

(9)   Smith, A. J.; Chang, Y. H.; Raidongia, K.; Chen, T. Y.; Li, L. J.; Huang, J. Molybdenum Sulfide Supported on Crumpled Graphene Balls for Electrocatalytic Hydrogen Production. *Adv. Energy Mater.* **2014**, *4* (14), 1–6. https://doi.org/10.1002/aenm.201400398.

(10)   Lin, J.; Peng, Z.; Wang, G.; Zakhidov, D.; Larios, E.; Yacaman, M. J.; Tour, J. M. Enhanced Electrocatalysis for Hydrogen Evolution Reactions from WS 2 Nanoribbons. *Adv. Energy Mater.* **2014**, *4* (10), 1–7. https://doi.org/10.1002/aenm.201301875.

(11)   Yin, Y.; Zhang, Y.; Gao, T.; Yao, T.; Zhang, X.; Han, J.; Wang, X.; Zhang, Z.; Xu, P.; Zhang, P.; et al. Synergistic Phase and Disorder Engineering in 1T-MoSe2 Nanosheets for Enhanced Hydrogen-Evolution Reaction. *Adv. Mater.* **2017**, *29* (28), 1–8. https://doi.org/10.1002/adma.201700311.

(12)   Laursen, A. B.; Kegnæs, S.; Dahl, S.; Chorkendorff, I. Molybdenum Sulfides —Efficient and Viable Materials for Electro - and Photoelectrocatalytic Hydrogen Evolution. *Energy Environ. Sci.* **2012**, *5* (2), 5577–5591. https://doi.org/10.1039/c2ee02618j.

(13)   Hinnemann, B.; Moses, P. G.; Bonde, J.; Jørgensen, K. P.; Nielsen, J. H.; Horch, S.; Chorkendorff, I.; Nørskov, J. K. Biomimetic Hydrogen Evolution: MoS 2 Nanoparticles as Catalyst for Hydrogen Evolution. *J. Am. Chem. Soc.* **2005**, *127* (15), 5308–5309. https://doi.org/10.1021/ja0504690.

(14)   Jaramillo, T. F.; Jorgensen, K. P.; Bonde, J.; Nielsen, J. H.; Horch, S.; Chorkendorff, I. Identification of Active Edge Sites for Electrochemical H2 Evolution from MoS2 Nanocatalysts. *Science (80-.).* **2007**, *317* (5834), 100–102. https://doi.org/10.1126/science.1141483.

(15)   Chia, X.; Eng, A. Y. S.; Ambrosi, A.; Tan, S. M.; Pumera, M. Electrochemistry of

Nanostructured Layered Transition-Metal Dichalcogenides. *Chem. Rev.* **2015**, *115* (21), 11941–11966. https://doi.org/10.1021/acs.chemrev.5b00287.

(16)   Tsai, C.; Chan, K.; Abild-Pedersen, F.; Nørskov, J. K. Active Edge Sites in MoSe2 and WSe2 Catalysts for the Hydrogen Evolution Reaction: A Density Functional Study. *Phys. Chem. Chem. Phys.* **2014**, *16* (26), 13156–13164. https://doi.org/10.1039/c4cp01237b.

(17)   Merki, D.; Fierro, S.; Vrubel, H.; Hu, X. Amorphous Molybdenum Sulfide Films as Catalysts for Electrochemical Hydrogen Production in Water. *Chem. Sci.* **2011**, *2*, 1262–1267. https://doi.org/10.1039/c1sc00117e.

(18)   Lu, A.; Yang, X.; Tseng, C.; Min, S.; Lin, S. High-Sulfur-Vacancy Amorphous Molybdenum Sulfide as a High Current Electrocatalyst in Hydrogen Evolution. *Small* **2016**, No. Cc, 1–8. https://doi.org/10.1002/smll.201602107.

(19)   Ye, Z.; Yang, J.; Li, B.; Shi, L.; Ji, H.; Song, L.; Xu, H. Amorphous Molybdenum Sulfide/Carbon Nanotubes Hybrid Nanospheres Prepared by Ultrasonic Spray Pyrolysis for Electrocatalytic Hydrogen Evolution. *Small* **2017**, *13* (21), 1–9. https://doi.org/10.1002/smll.201700111.

(20)   Geng, X.; Sun, W.; Wu, W.; Chen, B.; Al-hilo, A.; Benamara, M.; Zhu, H.; Watanabe, F.; Cui, J.; Chen, T. Pure and Stable Metallic Phase Molybdenum Disulfide Nanosheets for Hydrogen Evolution Reaction. *Nat. Commun.* **2016**, *7*, 1–7. https://doi.org/10.1038/ncomms10672.

(21)   Huang, Y. L.; Chen, Y.; Zhang, W.; Quek, S. Y.; Chen, C. H.; Li, L. J.; Hsu, W. T.; Chang, W. H.; Zheng, Y. J.; Chen, W.; et al. Bandgap Tunability at Single-Layer Molybdenum Disulphide Grain Boundaries. *Nat. Commun.* **2015**, *6*, 1–8. https://doi.org/10.1038/ncomms7298.

(22)   Lu, Z.; Zhu, W.; Yu, X.; Zhang, H.; Li, Y.; Sun, X.; Wang, X.; Wang, H.; Wang, J.; Luo, J.; et al. Ultrahigh Hydrogen Evolution Performance of Under-Water "Superaerophobic" MoS2 Nanostructured Electrodes. *Adv. Mater.* **2014**, *26* (17), 2683–2687. https://doi.org/10.1002/adma.201304759.

(23) Zhang, Z.; Wang, Y.; Leng, X.; Crespi, V. H.; Kang, F.; Lv, R. Controllable Edge Exposure of MoS2 for Efficient Hydrogen Evolution with High Current Density. *ACS Appl. Energy Mater.* **2018**, *1*, 1268–1275. https://doi.org/10.1021/acsaem.8b00010.

(24) Chen, Z.; Cummins, D.; Reinecke, B. N.; Clark, E.; Sunkara, M. K.; Jaramillo, T. F. Core-Shell MoO3-MoS2 Nanowires for Hydrogen Evolution. *Nano Lett.* **2011**, *11*, 4168–4175.

(25) Xie, J.; Qu, H.; Xin, J.; Zhang, X.; Cui, G.; Zhang, X.; Bao, J.; Tang, B.; Xie, Y. Defect-Rich MoS2 Nanowall Catalyst for Efficient Hydrogen Evolution Reaction. *Nano Res.* **2017**, *10* (4), 1178–1188. https://doi.org/10.1007/s12274-017-1421-x.

(26) Luo, Y.; Tang, L.; Khan, U.; Yu, Q.; Cheng, H.-M.; Zou, X.; Liu, B. Morphology and Surface Chemistry Engineering toward PH-Universal Catalysts for Hydrogen Evolution at High Current Density. *Nat. Commun.* **2019**, *10* (1), 1–9. https://doi.org/10.1038/s41467-018-07792-9.

(27) Liao, L.; Zhu, J.; Bian, X.; Zhu, L.; Scanlon, M. D.; Girault, H. H.; Liu, B. MoS2 Formed on Mesoporous Graphene as a Highly Active Catalyst for Hydrogen Evolution. *Adv. Funct. Mater.* **2013**, *23* (42), 5326–5333. https://doi.org/10.1002/adfm.201300318.

(28) Tang, Y. J.; Wang, Y.; Wang, X. L.; Li, S. L.; Huang, W.; Dong, L. Z.; Liu, C. H.; Li, Y. F.; Lan, Y. Q. Molybdenum Disulfide/Nitrogen-Doped Reduced Graphene Oxide Nanocomposite with Enlarged Interlayer Spacing for Electrocatalytic Hydrogen Evolution. *Adv. Energy Mater.* **2016**, *6* (12), 1–7. https://doi.org/10.1002/aenm.201600116.

(29) Cao, J.; Zhou, J.; Zhang, Y.; Zou, Y.; Liu, X. MoS2 Nanosheets Direct Supported on Reduced Graphene Oxide: An Advanced Electrocatalyst for Hydrogen Evolution Reaction. *PLoS One* **2017**, *12* (5), 1–10. https://doi.org/10.1371/journal.pone.0177258.

(30) Najafi, L.; Bellani, S.; Martín-García, B.; Oropesa-Nunez, R.; Del Rio Castillo, A. E.; Prato, M.; Moreels, I.; Bonaccorso, F. Solution-Processed Hybrid Graphene Flake/2H-MoS2Quantum Dot Heterostructures for Efficient Electrochemical Hydrogen Evolution. *Chem. Mater.* **2017**, *29* (14), 5782–5786. https://doi.org/10.1021/acs.chemmater.7b01897.

(31) Huang, J.; Chen, M.; Li, X.; Zhang, X.; Lin, L.; Liu, W.; Liu, Y. A Facile Layer-by-Layer

Fabrication of Three Dimensional MoS2-RGO-CNTs with High Performance for Hydrogen Evolution Reaction. *Electrochim. Acta* **2019**, *300*, 235–241. https://doi.org/10.1016/j.electacta.2019.01.107.

(32)   Li, H.; Tsai, C.; Koh, A. L.; Cai, L.; Contryman, A. W.; Fragapane, A. H.; Zhao, J.; Han, H. S.; Manoharan, H. C.; Abild-Pedersen, F.; et al. Activating and Optimizing MoS2 Basal Planes for Hydrogen Evolution through the Formation of Strained Sulphur Vacancies. *Nat. Mater.* **2015**, *15* (1), 48–53. https://doi.org/10.1038/nmat4465.

(33)   Madauß, L.; Zegkinoglou, I.; Vázquez Muiños, H.; Choi, Y. W.; Kunze, S.; Zhao, M. Q.; Naylor, C. H.; Ernst, P.; Pollmann, E.; Ochedowski, O.; et al. Highly Active Single-Layer MoS2 Catalysts Synthesized by Swift Heavy Ion Irradiation. *Nanoscale* **2018**, *10* (48), 22908–22916. https://doi.org/10.1039/c8nr04696d.

(34)   Voiry, D.; Salehi, M.; Silva, R.; Fujita, T.; Chen, M.; Asefa, T.; Shenoy, V. B.; Eda, G.; Chhowalla, M. Conducting MoS2 Nanosheets as Catalysts for Hydrogen Evolution Reaction. *Nano Lett.* **2013**, *13* (12), 6222–6227. https://doi.org/10.1021/nl403661s.

(35)   Xiang, Z. C.; Zhang, Z.; Xu, X. J.; Zhang, Q.; Yuan, C. MoS 2 Nanosheets Array on Carbon Cloth as a 3D Electrode for Highly Efficient Electrochemical Hydrogen Evolution. *Carbon N. Y.* **2016**, *98*, 84–89. https://doi.org/10.1016/j.carbon.2015.10.071.

(36)   Cai, L.; Cheng, W.; Yao, T.; Huang, Y.; Tang, F.; Liu, Q.; Liu, W.; Sun, Z.; Hu, F.; Jiang, Y.; et al. High-Content Metallic 1T Phase in MoS 2 -Based Electrocatalyst for Efficient Hydrogen Evolution. *J. Phys. Chem. C* **2017**, *121* (28), 15071–15077. https://doi.org/10.1021/acs.jpcc.7b03103.

(37)   Sun, K.; Liu, Y.; Pan, Y.; Zhu, H.; Zhao, J.; Zeng, L.; Liu, Z.; Liu, C. Targeted Bottom-up Synthesis of 1T-Phase MoS2 Arrays with High Electrocatalytic Hydrogen Evolution Activity by Simultaneous Structure and Morphology Engineering. *Nano Res.* **2018**, *11* (8), 4368–4379. https://doi.org/10.1007/s12274-018-2026-8.

(38)   Deng, J.; Li, H.; Xiao, J.; Tu, Y.; Deng, D.; Yang, H.; Tian, H.; Li, J.; Ren, P.; Bao, X. Triggering the Electrocatalytic Hydrogen Evolution Activity of the Inert Two-Dimensional

MoS2 Surface via Single-Atom Metal Doping. *Energy Environ. Sci.* **2015**, *8* (5), 1594–1601. https://doi.org/10.1039/c5ee00751h.

(39)   Ren, X.; Ma, Q.; Fan, H.; Pang, L.; Zhang, Y.; Yao, Y.; Ren, X.; Liu, S. A Se-Doped MoS 2 Nanosheet for Improved Hydrogen Evolution Reaction. *Chem. Commun.* **2015**, *51* (88), 15997–16000. https://doi.org/10.1039/c5cc06847a.

(40)   Liang, Y. Q.; Mao, J.; Cui, Z. D.; He, J. N.; Yang, X. J.; Li, Z. Y.; Zhang, X. M.; Li, B. B.; Zhu, S. L. 3D Tungsten-Doped MoS 2 Nanostructure: A Low-Cost, Facile Prepared Catalyst for Hydrogen Evolution Reaction. *J. Electrochem. Soc.* **2016**, *163* (5), H299–H304. https://doi.org/10.1149/2.0841605jes.

(41)   Gan, X.; Lv, R.; Wang, X.; Zhang, Z.; Fujisawa, K.; Lei, Y.; Huang, Z. H.; Terrones, M.; Kang, F. Pyrolytic Carbon Supported Alloying Metal Dichalcogenides as Free-Standing Electrodes for Efficient Hydrogen Evolution. *Carbon N. Y.* **2018**, *132*, 512–519. https://doi.org/10.1016/j.carbon.2018.02.025.

(42)   Liu, P.; Zhu, J.; Zhang, J.; Tao, K.; Gao, D.; Xi, P. Active Basal Plane Catalytic Activity and Conductivity in Zn Doped MoS2 Nanosheets for Efficient Hydrogen Evolution. *Electrochim. Acta* **2018**, *260*, 24–30. https://doi.org/10.1016/j.electacta.2017.11.080.

(43)   Xie, J.; Zhang, J.; Li, S.; Grote, F.; Zhang, X.; Zhang, H.; Wang, R.; Lei, Y.; Pan, B.; Xie, Y. Controllable Disorder Engineering in Oxygen-Incorporated MoS2 Ultrathin Nanosheets for Efficient Hydrogen Evolution. *J. Am. Chem. Soc.* **2013**, *135* (47), 17881–17888. https://doi.org/10.1021/ja408329q.

(44)   Nikam, R. D.; Lu, A. Y.; Sonawane, P. A.; Kumar, U. R.; Yadav, K.; Li, L. J.; Chen, Y. T. Three-Dimensional Heterostructures of MoS2 Nanosheets on Conducting MoO2 as an Efficient Electrocatalyst to Enhance Hydrogen Evolution Reaction. *ACS Appl. Mater. Interfaces* **2015**, *7* (41), 23328–23335. https://doi.org/10.1021/acsami.5b07960.

(45)   Wang, J.; Wang, W.; Wang, Z.; Chen, J. G.; Liu, C. J. Porous MS 2 /MO 2 (M = W, Mo) Nanorods as Efficient Hydrogen Evolution Reaction Catalysts. *ACS Catal.* **2016**, *6* (10), 6585–6590. https://doi.org/10.1021/acscatal.6b01927.

(46) Liu, A.; Zhao, L.; Zhang, J.; Lin, L.; Wu, H. Solvent-Assisted Oxygen Incorporation of Vertically Aligned MoS2 Ultrathin Nanosheets Decorated on Reduced Graphene Oxide for Improved Electrocatalytic Hydrogen Evolution. *ACS Appl. Mater. Interfaces* **2016**, *8* (38), 25210–25218. https://doi.org/10.1021/acsami.6b06031.

(47) Hu, T.; Bian, K.; Tai, G.; Zeng, T.; Wang, X.; Huang, X.; Xiong, K.; Zhu, K. Oxidation-Sulfidation Approach for Vertically Growing MoS2 Nanofilms Catalysts on Molybdenum Foils as Efficient HER Catalysts. *J. Phys. Chem. C* **2016**, *120* (45), 25843–25850. https://doi.org/10.1021/acs.jpcc.6b08120.

(48) Tedstone, A. A.; Lewis, D. J.; O'Brien, P. Synthesis, Properties, and Applications of Transition Metal-Doped Layered Transition Metal Dichalcogenides. *Chem. Mater.* **2016**, *28* (7), 1965–1974. https://doi.org/10.1021/acs.chemmater.6b00430.

(49) Ekspong, J.; Sharifi, T.; Shchukarev, A.; Klechikov, A.; Wågberg, T.; Gracia-Espino, E. Stabilizing Active Edge Sites in Semicrystalline Molybdenum Sulfide by Anchorage on Nitrogen-Doped Carbon Nanotubes for Hydrogen Evolution Reaction. *Adv. Funct. Mater.* **2016**, *26* (37), 6766–6776. https://doi.org/10.1002/adfm.201601994.

(50) Lee, K. E.; Sasikala, S. P.; Lee, H. J.; Lee, G. Y.; Koo, S. H.; Yun, T.; Jung, H. J.; Kim, I. H.; Kim, S. O. Amorphous Molybdenum Sulfide Deposited Graphene Liquid Crystalline Fiber for Hydrogen Evolution Reaction Catalysis. *Part. Part. Syst. Charact.* **2017**, *34* (9), 1–5. https://doi.org/10.1002/ppsc.201600375.

(51) Pham, K. C.; Chang, Y. H.; McPhail, D. S.; Mattevi, C.; Wee, A. T. S.; Chua, D. H. C. Amorphous Molybdenum Sulfide on Graphene-Carbon Nanotube Hybrids as Highly Active Hydrogen Evolution Reaction Catalysts. *ACS Appl. Mater. Interfaces* **2016**, *8* (9), 5961–5971. https://doi.org/10.1021/acsami.5b09690.

(52) Bao, X. Q.; Petrovykh, D. Y.; Alpuim, P.; Stroppa, D. G.; Guldris, N.; Fonseca, H.; Costa, M.; Gaspar, J.; Jin, C.; Liu, L. Amorphous Oxygen-Rich Molybdenum Oxysulfide Decorated p-Type Silicon Microwire Arrays for Efficient Photoelectrochemical Water Reduction. *Nano Energy* **2015**, *16*, 130–142. https://doi.org/10.1016/j.nanoen.2015.06.014.

(53) Fominski, V. Y.; Romanov, R. I.; Fominski, D. V.; Shelyakov, A. V. Regulated Growth of Quasi-Amorphous MoSx Thin-Film Hydrogen Evolution Catalysts by Pulsed Laser Deposition of Mo in Reactive H2S Gas. *Thin Solid Films* **2017**, *642* (August), 58–68. https://doi.org/10.1016/j.tsf.2017.09.020.

(54) Wang, R.; Sun, P.; Wang, H.; Wang, X. Pulsed Laser Deposition of Amorphous Molybdenum Disulfide Films for Efficient Hydrogen Evolution Reaction. *Electrochim. Acta* **2017**, *258*, 876–882. https://doi.org/10.1016/j.electacta.2017.11.138.

(55) Fominski, V. Y.; Romanov, R. I.; Fominski, D. V.; Dzhumaev, P. S.; Troyan, I. A. Normal and Grazing Incidence Pulsed Laser Deposition of Nanostructured MoSxhydrogen Evolution Catalysts from a MoS2target. *Opt. Laser Technol.* **2018**, *102*, 74–84. https://doi.org/10.1016/j.optlastec.2017.12.028.

(56) Ting, L. R. L.; Deng, Y.; Ma, L.; Zhang, Y. J.; Peterson, A. A.; Yeo, B. S. Catalytic Activities of Sulfur Atoms in Amorphous Molybdenum Sulfide for the Electrochemical Hydrogen Evolution Reaction. *ACS Catal.* **2016**, *6* (2), 861–867. https://doi.org/10.1021/acscatal.5b02369.

(57) Tran, P. D.; Tran, T. V; Orio, M.; Torelli, S.; Truong, Q. D.; Nayuki, K.; Sasaki, Y.; Chiam, S. Y.; Yi, R.; Honma, I.; et al. Coordination Polymer Structure and Revisited Hydrogen Evolution Catalytic Mechanism for Amorphous Molybdenum Sulfide. *Nat. Mater.* **2016**, *15* (March). https://doi.org/10.1038/NMAT4588.

(58) Escalera-lópez, D.; Lou, Z.; Rees, N. V. Benchmarking the Activity, Stability, and Inherent Electrochemistry of Amorphous Molybdenum Sulfide for Hydrogen Production. *Adv. Energy Mater.* **2019**, *9* (8). https://doi.org/10.1002/aenm.201802614.

(59) Tian, M.; Dyck, O.; Ge, J.; Duscher, G. Measuring the Areal Density of Nanomaterials by Electron Energy-Loss Spectroscopy. *Ultramicroscopy* **2019**, *196* (March 2018), 154–160. https://doi.org/10.1016/j.ultramic.2018.10.009.

(60) Belianinov, A.; Burch, M. J.; Kim, S.; Tan, S.; Hlawacek, G.; Ovchinnikova, O. S. Noble Gas Ion Beams in Materials Science for Future Applications and Devices. *MRS Bull.* **2017**,

42 (9), 660–666. https://doi.org/10.1557/mrs.2017.185.

(61)   Hlawacek, G.; Gölzhäuser, A. *Helium Ion Microscopy*; 2016.

(62)   Wirtz, T.; Dowsett, D.; Philipp, P. SIMS on the Helium Ion Microscope: A Powerful Tool for High-Resolution High-Sensitivity Nano-Analytics. *Microsc. Microanal.* **2016**, *22* (S3), 160–161. https://doi.org/10.1007/978-3-319-41990-9_13.

(63)   Cao, P.; Peng, J.; Liu, S.; Cui, Y.; Hu, Y.; Chen, B.; Li, J.; Zhai, M. Tuning the Composition and Structure of Amorphous Molybdenum Sulfide/Carbon Black Nanocomposites by Radiation Technique for Highly Efficient Hydrogen Evolution. *Sci. Rep.* **2017**, *7* (1), 1–11. https://doi.org/10.1038/s41598-017-16015-y.

(64)   Chen, R.; Yang, C.; Cai, W.; Wang, H. Y.; Miao, J.; Zhang, L.; Chen, S.; Liu, B. Use of Platinum as the Counter Electrode to Study the Activity of Nonprecious Metal Catalysts for the Hydrogen Evolution Reaction. *ACS Energy Lett.* **2017**, *2* (5), 1070–1075. https://doi.org/10.1021/acsenergylett.7b00219.

(65)   Passoni, L.; Criante, L.; Fumagalli, F.; Scotognella, F.; Lanzani, G.; Di Fonzo, F. Self-Assembled Hierarchical Nanostructures for High-Efficiency Porous Photonic Crystals. *ACS Nano* **2014**, *8* (12), 12167–12174. https://doi.org/10.1021/nn5037202.

(66)   Bellani, S.; Ghadirzadeh, A.; Meda, L.; Savoini, A.; Tacca, A.; Marra, G.; Meira, R.; Morgado, J.; Di Fonzo, F.; Antognazza, M. R. Hybrid Organic/Inorganic Nanostructures for Highly Sensitive Photoelectrochemical Detection of Dissolved Oxygen in Aqueous Media. *Adv. Funct. Mater.* **2015**, *25* (28), 4531–4538. https://doi.org/10.1002/adfm.201500701.

(67)   Perego, A.; Giuffredi, G.; Mazzolini, P.; Colombo, M.; Brescia, R.; Prato, M.; Sabarirajan, D. C.; Zenyuk, I. V.; Bossola, F.; Dal Santo, V.; et al. Hierarchical TiN Nanostructured Thin Film Electrode for Highly Stable PEM Fuel Cells. *ACS Appl. Energy Mater.* **2019**. https://doi.org/10.1021/acsaem.8b02030.

(68)   Passoni, L.; Ghods, F.; Docampo, P.; Abrusci, A.; Martí-Rujas, J.; Ghidelli, M.; Divitini, G.; Ducati, C.; Binda, M.; Guarnera, S.; et al. Hyperbranched Quasi-1d Nanostructures for

Solid-State Dye-Sensitized Solar Cells. *ACS Nano* **2013**, *7* (11), 10023–10031. https://doi.org/10.1021/nn403979h.

(69)   Balandeh, M.; Mezzetti, A.; Tacca, A.; Leonardi, S.; Marra, G.; Divitini, G.; Ducati, C.; Meda, L.; Di Fonzo, F. Quasi-1D Hyperbranched WO $_3$ Nanostructures for Low-Voltage Photoelectrochemical Water Splitting. *J. Mater. Chem. A* **2015**, *3* (11), 6110–6117. https://doi.org/10.1039/C4TA06786J.

(70)   Mahjouri-Samani, M.; Tian, M.; Puretzky, A. A.; Chi, M.; Wang, K.; Duscher, G.; Rouleau, C. M.; Eres, G.; Yoon, M.; Lasseter, J.; et al. Nonequilibrium Synthesis of TiO2 Nanoparticle "Building Blocks" for Crystal Growth by Sequential Attachment in Pulsed Laser Deposition. *Nano Lett.* **2017**, *17* (8), 4624–4633. https://doi.org/10.1021/acs.nanolett.7b01047.

(71)   Wood, R.; Leboeuf, J.; Geohegan, D.; Puretzky, A.; Chen, K. Dynamics of Plume Propagation and Splitting during Pulsed-Laser Ablation of Si in He and Ar. *Phys. Rev. B - Condens. Matter Mater. Phys.* **1998**, *58* (3), 1533–1543. https://doi.org/10.1103/PhysRevB.58.1533.

(72)   Wood, R. F.; Leboeuf, J. N.; Chen, K. R.; Geohegan, D. B.; Puretzky, A. A. Dynamics of Plume Propagation, Splitting, and Nanoparticle Formation during Pulsed-Laser Ablation. *Appl. Surf. Sci.* **1998**, *127–129*, 151–158. https://doi.org/10.1016/S0169-4332(97)00625-9.

(73)   Benck, J. D.; Chen, Z.; Kuritzky, L. Y.; Forman, A. J.; Jaramillo, T. F. Amorphous Molybdenum Sulfide Catalysts for Electrochemical Hydrogen Production: Insights into the Origin of Their Catalytic Activity. *ACS Catal.* **2012**, *2*, 2–9.

(74)   Lee, S. C.; Benck, J. D.; Tsai, C.; Park, J.; Koh, A. L.; Abild-Pedersen, F.; Jaramillo, T. F.; Sinclair, R. Chemical and Phase Evolution of Amorphous Molybdenum Sulfide Catalysts for Electrochemical Hydrogen Production. *ACS Nano* **2016**, *10* (1), 624–632. https://doi.org/10.1021/acsnano.5b05652.

(75)   Vrubel, H.; Hu, X. Growth and Activation of an Amorphous Molybdenum Sulfide Hydrogen Evolving Catalyst. *ACS Catal.* **2013**, *3* (9), 2002–2011.

https://doi.org/10.1021/cs400441u.

(76)   Davoodi, A.; Pakshir, M.; Babaiee, M.; Ebrahimi, G. R. A Comparative H2S Corrosion Study of 304L and 316L Stainless Steels in Acidic Media. *Corros. Sci.* **2011**, *53* (1), 399–408. https://doi.org/10.1016/j.corsci.2010.09.050.

(77)   Conway, B. E.; Bai, L. Determination of Adsorption of OPD H Species in the Cathodic Hydrogen Evolution Reaction at Pt in Relation to Electrocatalysis. *J. Electroanal. Chem.* **1986**, *198* (1), 149–175. https://doi.org/10.1016/0022-0728(86)90033-1.

(78)   De Chialvo, M. R. G.; Chialvo, A. C. Hydrogen Evolution Reaction : Analysis of the Volmer-Heyrovsky-Tafel Mechanism with a Generalized Adsorption ... Hydrogen Evolution Reaction : Analysis of the Volmer-Heyrovsky-Tafel. *J. Electroanal. Chem.* **1994**, *372* (February), 209–223. https://doi.org/10.1016/0022-0728(93)03043-O.

(79)   Shinagawa, T.; Garcia-esparza, A. T.; Takanabe, K. Insight on Tafel Slopes from a Microkinetic Analysis of Aqueous Electrocatalysis for Energy Conversion. *Nat. Sci. Reports* **2015**, No. May, 1–21. https://doi.org/10.1038/srep13801.

(80)   Gerosa, M.; Bottani, C. E. Multiple Light Scattering and Near-Field Effects in a Fractal Treelike Ensemble of Dielectric Nanoparticles. *Phys. Rev. B - Condens. Matter Mater. Phys.* **2013**, *87* (19), 1–8. https://doi.org/10.1103/PhysRevB.87.195312.

(81)   Kibsgaard, J.; Jaramillo, T. F.; Besenbacher, F. Building an Appropriate Active-Site Motif into a Hydrogen-Evolution Catalyst with Thiomolybdate [Mo3S13]2− Clusters. *Nat. Chem.* **2014**, *6* (3), 248–253. https://doi.org/10.1038/nchem.1853.

(82)   Bard, A. J.; Faulkner, L. R. *Electrochemical Methods: Fundamentals and Applications*, Second Edi.; John Wiley & Sons, Inc., 2001; Vol. 8. https://doi.org/10.1016/B978-0-08-098353-0.00003-8.

(83)   Ling, L.; Wang, C.; Zhang, K.; Li, T.; Tang, L.; Li, C.; Wang, L.; Xu, Y.; Song, Q.; Yao, Y. Controlled Growth of MoS2 Nanopetals and Their Hydrogen Evolution Performance. *RSC Adv.* **2016**, *6* (22), 18483–18489. https://doi.org/10.1039/c5ra24908b.

(84)   Kong, X.; Shen, X.; Zhang, C.; Oliaee, S. N.; Peng, Z. Engineering Active Sites of Two-Dimensional MoS2 Nanosheets for Improving Hydrogen Evolution. *Inorg. Chem. Front.* **2016**, *3* (11), 1376–1380. https://doi.org/10.1039/c6qi00334f.

(85)   Gao, M.-R.; Chan, M. K. Y.; Sun, Y. Edge-Terminated Molybdenum Disulfide with a 9.4-Å Interlayer Spacing for Electrochemical Hydrogen Production. *Nat. Commun.* **2015**, *6* (May), 7493. https://doi.org/10.1038/ncomms8493.

(86)   Kunhiraman, A. K.; Ramanathan, S.; Pullithadathil, B. Enlarged Interlayer Spaced Molybdenum Disulfide Supported on Nanocarbon Hybrid Network for Efficient Hydrogen Evolution Reaction. *Electrochim. Acta* **2018**, *264*, 329–340. https://doi.org/10.1016/j.electacta.2018.01.135.

(87)   Gao, G.; Sun, Q.; Du, A. Activating Catalytic Inert Basal Plane of Molybdenum Disulfide to Optimize Hydrogen Evolution Activity via Defect Doping and Strain Engineering. *J. Phys. Chem. C* **2016**, *120* (30), 16761–16766. https://doi.org/10.1021/acs.jpcc.6b04692.

(88)   Bernède, J. C. About the Preferential Sputtering of Chalcogen from Transition Metal Dichalcogenide Compounds and the Determination of Compound Stoichiometry from XPS Peak Positions. *Appl. Surf. Sci.* **2001**, *171* (1–2), 15–20. https://doi.org/10.1016/S0169-4332(00)00535-3.

(89)   Grigoriev, S. N.; Fominski, V. Y.; Gnedovets, A. G.; Romanov, R. I. Experimental and Numerical Study of the Chemical Composition of WSex Thin Films Obtained by Pulsed Laser Deposition in Vacuum and in a Buffer Gas Atmosphere. *Appl. Surf. Sci.* **2012**, *258* (18), 7000–7007. https://doi.org/10.1016/j.apsusc.2012.03.153.

(90)   Brien, M. O.; Mcevoy, N.; Hanlon, D.; Hallam, T.; Coleman, J. N.; Duesberg, G. S. Mapping of Low-Frequency Raman Modes in CVD-Grown Transition Metal Dichalcogenides : Layer Number , Stacking Orientation and Resonant Effects. *Nat. Sci. Reports* **2016**, 1–11. https://doi.org/10.1038/srep19476.

(91)   Liang, L.; Zhang, J.; Sumpter, B. G.; Tan, Q.; Tan, P. Low-Frequency Shear and Layer-Breathing Modes in Raman Scattering of Two- Dimensional Materials. *ACS Nano* **2017**,

11, 11777–11802. https://doi.org/10.1021/acsnano.7b06551.

(92) Deng, Y.; Ting, L. R. L.; Neo, P. H. L.; Zhang, Y. J.; Peterson, A. A.; Yeo, B. S. Operando Raman Spectroscopy of Amorphous Molybdenum Sulfide (MoSx) during the Electrochemical Hydrogen Evolution Reaction: Identification of Sulfur Atoms as Catalytically Active Sites for H+ Reduction. *ACS Catal.* **2016**, *6* (11), 7790–7798. https://doi.org/10.1021/acscatal.6b01848.

(93) Weber, T.; Muijsers, J. C.; Niemantsverdriet, J. W. Structure of Amorphous MoS3. *J. Phys. Chem.* **1995**, *99* (22), 9194–9200. https://doi.org/10.1021/j100022a037.

(94) Vasilopoulou, M.; Douvas, A. M.; Georgiadou, D. G.; Palilis, L. C.; Kennou, S.; Sygellou, L.; Soultati, A.; Kostis, I.; Papadimitropoulos, G.; Davazoglou, D.; et al. The Influence of Hydrogenation and Oxygen Vacancies on Molybdenum Oxides Work Function and Gap States for Application in Organic Optoelectronics. *J. Am. Chem. Soc.* **2012**, *134* (39), 16178–16187. https://doi.org/10.1021/ja3026906.

(95) Casalongue, H. G. S.; Benck, J. D.; Tsai, C.; Karlsson, R. K. B.; Kaya, S.; Ng, M. L.; Pettersson, L. G. M.; Abild-Pedersen, F.; Nørskov, J. K.; Ogasawara, H.; et al. Operando Characterization of an Amorphous Molybdenum Sulfide Nanoparticle Catalyst during the Hydrogen Evolution Reaction. *J. Phys. Chem. C* **2014**, *118* (50), 29252–29259. https://doi.org/10.1021/jp505394e.

(96) Gong, L.; Haur, S. C. On Demand Rapid Patterning of Colored Amorphous Molybdenum Oxide Using a Focused Laser Beam. *J. Mater. Chem. C* **2017**, *5* (8), 2090–2097. https://doi.org/10.1039/c6tc04580d.

(97) Sinclair, R.; Benck, J. D.; Lee, S. C.; Abild-Pedersen, F.; Jaramillo, T. F.; Tsai, C.; Park, J.; Koh, A. L. Chemical and Phase Evolution of Amorphous Molybdenum Sulfide Catalysts for Electrochemical Hydrogen Production. *ACS Nano* **2015**, *10* (1), 624–632. https://doi.org/10.1021/acsnano.5b05652.

(98) Schrader, G. L.; Cheng, C. P. In Situ Laser Raman Spectroscopy of the Sulfiding of Mo γ-Al2O3 Catalysts. *J. Catal.* **1983**, *80* (2), 369–385. https://doi.org/10.1016/0021-

9517(83)90262-2.

(99)   Nevskaya, E. Y.; Gorichev, I. G.; Izotov, A. D.; Zaitsev, B. E.; Al, K. M.; Kutepov, A. M. Kinetics of Molybdenum(VI) Oxide Dissolution in Sulfuric Acid Solutions. *Theor. Found. Chem. Eng.* **2004**, *38* (3), 337–342.

(100) Guo, J.; Li, F.; Sun, Y.; Zhang, X.; Tang, L. Oxygen-Incorporated MoS2 Ultrathin Nanosheets Grown on Graphene for Efficient Electrochemical Hydrogen Evolution. *J. Power Sources* **2015**, *291*, 195–200. https://doi.org/10.1016/j.jpowsour.2015.05.034.

(101) Dolinska, J.; Chidambaram, A.; Adamkiewicz, W.; Estili, M.; Lisowski, W.; Iwan, M.; Palys, B.; Sudholter, E. J. R.; Marken, F.; Opallo, M.; et al. Synthesis and Characterization of Porous Carbon–MoS ₂ Nanohybrid Materials: Electrocatalytic Performance towards Selected Biomolecules. *J. Mater. Chem. B* **2016**, *4* (8), 1448–1457. https://doi.org/10.1039/C5TB02175H.

(102) Wang, S.; Tu, J.; Yuan, Y.; Ma, R.; Jiao, S. Sodium Modified Molybdenum Sulfide via Molten Salt Electrolysis as an Anode Material for High Performance Sodium-Ion Batteries. *Phys. Chem. Chem. Phys.* **2016**, *18* (4), 3204–3213. https://doi.org/10.1039/c5cp07007d.

(103) Li, X.; Jiang, Y.; Jia, L.; Wang, C. MoO2 Nanoparticles on Reduced Graphene Oxide/Polyimide-Carbon Nanotube Film as Efficient Hydrogen Evolution Electrocatalyst. *J. Power Sources* **2016**, *304*, 146–154. https://doi.org/10.1016/j.jpowsour.2015.11.013.

(104) Chen, Y.; Yu, G.; Chen, W.; Liu, Y.; Li, G. D.; Zhu, P.; Tao, Q.; Li, Q.; Liu, J.; Shen, X.; et al. Highly Active, Nonprecious Electrocatalyst Comprising Borophene Subunits for the Hydrogen Evolution Reaction. *J. Am. Chem. Soc.* **2017**, *139* (36), 12370–12373. https://doi.org/10.1021/jacs.7b06337.

(105) Babic, U.; Suermann, M.; Büchi, F. N.; Gubler, L.; Schmidt, T. J. Critical Review—Identifying Critical Gaps for Polymer Electrolyte Water Electrolysis Development. *J. Electrochem. Soc.* **2017**, *164* (4), F387–F399. https://doi.org/10.1149/2.1441704jes.

(106) Zhou, H.; Yu, F.; Sun, J.; Zhu, Z.; Nielsen, R. J.; He, R.; Bao, J.; Goddard III, W. A.; Huang, Y.; Chen, S.; et al. Efficient Hydrogen Evolution by Ternary Molybdenum Sulfoselenide

Particles on Self-Standing Porous Nickel Diselenide Foam. *Nat. Commun.* **2016**, *7* (1), 1–7. https://doi.org/10.1038/ncomms12765.

(107) Lin, L.; Miao, N.; Wen, Y.; Zhang, S.; Ghosez, P.; Sun, Z.; Allwood, D. A. Sulfur-Depleted Monolayered Molybdenum Disulfide Nanocrystals for Superelectrochemical Hydrogen Evolution Reaction. *ACS Nano* **2016**, *10* (9), 8929–8937. https://doi.org/10.1021/acsnano.6b04904.

(108) Li, D. J.; Maiti, U. N.; Lim, J.; Choi, D. S.; Lee, W. J.; Oh, Y.; Lee, G. Y.; Kim, S. O. Molybdenum Sulfide/N-Doped CNT Forest Hybrid Catalysts for High-Performance Hydrogen Evolution Reaction. *Nano Lett.* **2014**, *14* (3), 1228–1233. https://doi.org/10.1021/nl404108a.

(109) Yang, L.; Mukhopadhyay, A.; Jiao, Y.; Hamel, J.; Benamara, M.; Xing, Y.; Zhu, H. Aligned and Stable Metallic MoS2 on Plasma-Treated Mass Transfer Channels for the Hydrogen Evolution Reaction. *J. Mater. Chem. A* **2017**, *5* (48), 25359–25367. https://doi.org/10.1039/c7ta08400e.